Monthly Notices
of the
ROYAL ASTRONOMICAL SOCIETY

MNRAS **486,** 1094–1122 (2019)
Advance Access publication 2019 March 29

doi:10.1093/mnras/stz902

Non-equilibrium chemistry and destruction of CO by X-ray flares

Jonathan Mackey [1,2,3★] Stefanie Walch,[3] Daniel Seifried [3] Simon C. O. Glover,[4] Richard Wünsch [5] and Felix Aharonian [1,2,6]

[1] *Centre for AstroParticle Physics and Astrophysics, DIAS Dunsink Observatory, Dunsink Lane, D15 XR2R Dublin 15, Ireland*
[2] *Dublin Institute for Advanced Studies, Astronomy & Astrophysics Section, 31 Fitzwilliam Place, D02 XF86 Dublin 2, Ireland*
[3] *I. Physikalisches Institut, Universität Köln, Zülpicher Str. 77, D-50937 Köln, Germany*
[4] *Zentrum für Astronomie, Institut für Theoretische Astrophysik, Universität Heidelberg, Albert-Ueberle-Str. 2, D-69120 Heidelberg, Germany*
[5] *Astronomical Institute, Czech Academy of Sciences, Boční II 1401, CZ-141 00 Prague, Czech Republic*
[6] *Max-Planck-Institut für Kernphysik, PO Box 103980, D-69029 Heidelberg, Germany*

Accepted 2019 March 25. Received 2018 December 11; in original form 2018 March 27

ABSTRACT

Sources of X-rays such as active galactic nuclei and X-ray binaries are often variable by orders of magnitude in luminosity over time-scales of years. During and after these flares the surrounding gas is out of chemical and thermal equilibrium. We introduce a new implementation of X-ray radiative transfer coupled to a time-dependent chemical network for use in 3D magnetohydrodynamical simulations. A static fractal molecular cloud is irradiated with X-rays of different intensity, and the chemical and thermal evolution of the cloud are studied. For a simulated 10^5 $M_\odot$ fractal cloud, an X-ray flux <0.01 erg cm^{-2} s^{-1} allows the cloud to remain molecular, whereas most of the CO and H_2 are destroyed for a flux of ≥ 1 erg cm^{-2} s^{-1}. The effects of an X-ray flare, which suddenly increases the X-ray flux by $10^5\times$, are then studied. A cloud exposed to a bright flare has 99 per cent of its CO destroyed in 10–20 yr, whereas it takes $>10^3$ yr for 99 per cent of the H_2 to be destroyed. CO is primarily destroyed by locally generated far-UV emission from collisions between non-thermal electrons and H_2; He^+ only becomes an important destruction agent when the CO abundance is already very small. After the flare is over, CO re-forms and approaches its equilibrium abundance after 10^3–10^5 yr. This implies that molecular clouds close to Sgr A* in the Galactic Centre may still be out of chemical equilibrium, and we predict the existence of clouds near flaring X-ray sources in which CO has been mostly destroyed but H is fully molecular.

Key words: astrochemistry – radiative transfer – methods: numerical – ISM: clouds – X-rays: general – X-rays: ISM.

1 INTRODUCTION

Heating and ionization by X-rays and cosmic rays (CRs) are known to be a key process in setting the temperature and ionization state of interstellar gas (Spitzer & Tomasko 1968; Dalgarno & McCray 1972; Shull & van Steenberg 1985). X-rays with energy >1 keV can propagate deeper into molecular clouds than ultraviolet (UV) or optical radiation because their interaction cross-section is smaller and decreases with increasing photon energy. The ionizations induced by X-rays that are absorbed in a molecular cloud can strongly affect the chemical balance of the cloud by heating it and increasing the electron fraction (Lepp & McCray 1983; Maloney, Hollenbach & Tielens 1996). The sources of X-rays, especially non-thermal sources related to X-ray binaries or active galactic nuclei (AGN), tend to be strongly variable on time-scales from minutes to years depending on the size of the emitting region.

Even mostly inactive black hole sources such as Sgr A* in the Galactic Centre occasionally have giant flares where the X-ray luminosity increases by a factor of 10^3–10^6 for a few years at a time. Ponti et al. (2010) studied X-ray reflection from molecular clouds around the Galactic Centre in the iron K-shell lines. They find that the luminosity of Sgr A$*$ has been at $L_x \lesssim 10^{35}$ erg s^{-1} for the past 60–90 yr, but that a bright flare with $L_x \approx 1.4\times10^{39}$ erg s^{-1} occurred about 100 yr ago, with a duration of at least 10 yr (see also Sunyaev, Markevitch & Pavlinsky 1993; Koyama et al. 1996; Sunyaev & Churazov 1998; Churazov et al. 2017a). The scattering of X-rays in molecular clouds has been studied using Monte Carlo radiative-transfer simulations (Odaka et al. 2011; Molaro et al. 2016; Molaro, Khatri & Sunyaev 2016; Walls et al. 2016) and shown to be a powerful diagnostic of the incident X-ray flux on a cloud. The inferred luminosity is still far below the Eddington luminosity for

★ E-mail: jmackey@cp.dias.ie

Sgr A∗, but is $\gtrsim 10^4$ times brighter than its current luminosity in X-rays.

X-ray binaries are also powerful sources during their active periods (e.g. GRS 1915+105 with $L_x \approx 10^{39}$ erg s^{-1} for ∼10 yr, see Punsly & Rodriguez 2013). This shows that molecular clouds close to black holes or luminous X-ray binaries are subject to occasional bright X-ray irradiation, which may affect their thermal and chemical state (Churazov et al. 2017c; Krivonos et al. 2017). If these flares are frequent enough (Churazov et al. 2017b), then the clouds could spend most of their time out of chemical and thermal equilibrium (Moser et al. 2017).

Bright X-ray sources are also usually sites of efficient CR production. For example, the link between CR production and supernova remnants is now well established (Aharonian 2013), the Galactic Centre is a bright and diffuse source of γ-rays produced by CRs (H. E. S. S. Collaboration 2017), and *FERMI* has detected hundreds of AGN at 0.1–100 GeV energy (Ackermann et al. 2011). Like X-rays, CRs propagate deep into molecular clouds, but their interaction with atoms produce γ-rays as a by-product of nuclear reactions. For both X-ray and CR interaction with matter the main ionizing and heating agents are so-called *secondary electrons*, produced when high-energy photons or CRs ionize a heavy element. These electrons have large kinetic energy, comparable to that of the ionizing photon, and so they ionize and heat molecules and atoms as they lose energy through collisional interactions (e.g. Maloney et al. 1996). This means that the effects of an elevated CR energy density and of an elevated X-ray radiation field can be difficult to distinguish, and one must either look deeply into the abundances of rare chemical species or consider the different attenuation of CRs and X-rays with column density. X-rays propagate in straight lines at the speed of light and are simply attenuated, whereas CRs follow trajectories determined by the local magnetic field and on large enough scales their propagation follows a diffusion equation (Girichidis et al. 2016; Pfrommer et al. 2017).

Under the assumption that X-rays are unimportant for the chemistry, Caselli et al. (1998) showed that the electron fraction and CR ionization rate within a dense cloud can be inferred from abundance ratios of HCO^+, CO, and DCO^+ (the deuterated form of HCO^+). Vaupré et al. (2014) studied a molecular cloud being impacted by the W28 supernova remnant, using the observed molecular lines to constrain the CR ionization rate to be >100 times the background Galactic rate. Clark et al. (2013) compared observations of the Galactic Centre cloud G0.253+0.016 with simulations using different CR ionization rates, finding that it too should have a CR energy density >100 times the background Galactic value. Investigating extreme environments, Bisbas, Papadopoulos & Viti (2015) studied how CO is destroyed in molecular clouds as the CR energy density increases, using chemical equilibrium calculations of photodissociation regions (PDR). They found that the number ratio of CO to H_2 decreases strongly with increasing CR energy density, because CO is effectively destroyed by He^+ ions created by CR ionization. This was followed up with 3D simulations of fractal clouds exposed to different CR energy densities (Bisbas et al. 2017), confirming their previous results. Gong, Ostriker & Wolfire (2017) also studied PDR chemistry with elevated CR energy density, finding that grain-assisted recombination of He^+ limits the effectiveness of CO destruction by CRs.

Meijerink, Spaans & Israel (2006) studied X-ray dominated regions (XDR) and PDRs including elevated CR ionization and heating rates. For a cloud exposed to high-X-ray flux, the XDR is most of the cloud volume, the PDR traces the cloud surface, and CRs affect both the surface and interior of a cloud. They found that line ratios of HCN, CO, and HCO^+ can be used, with high-J lines of CO, to distinguish between X-ray- and CR-irradiated clouds. Subsequently, Meijerink et al. (2011) found that OH, OH^+, H_2O, H_2O^+, and H_3O^+ can also be used to discriminate CR and X-ray irradiation.

Most previous chemical studies of X-ray irradiated MCs assume chemical and/or thermal equilibrium, similar to PDR models (e.g. Maloney et al. 1996; Meijerink & Spaans 2005; Hocuk & Spaans 2010). The codes developed for these projects therefore cannot capture the time-dependent chemistry and thermodynamics that occurs within a molecular cloud irradiated by a time-dependent X-ray radiation field. A recent departure from this is the study of Cleeves et al. (2017), who investigated variable $H^{13}CO^+$ emission (observed in a protstellar disc) as a consequence of a time-varying X-ray irradiation. So far there are no studies of the time-dependent chemistry of, for example, the molecular clouds near Sgr A*, which arises from the recent flare.

Here we introduce a non-equilibrium code that couples X-ray irradiation to chemistry and thermodynamics (and potentially hydrodynamics) of molecular gas, using a simplified chemical network of 17 species. The treatment of X-ray radiation, the chemical network, and coupling to the FLASH code is described in Section 2. Tests of the network using 1D, constant-density slabs are presented in Section 3. Section 4 introduces the modelling of a fractal cloud in 3D using the FLASH code, embedded in a homogeneous and isotropic background radiation field. The equilibrium state of the gas for different X-ray radiation intensities is obtained, and the states compared with each other. In Section 5, the equilibrium state is disturbed by X-ray flares of duration 1–100 yr, and we show the time-dependent effects of the flares on the chemical abundances and gas temperature during and after the flare event. Our results are discussed in Section 6 and our conclusions presented in Section 7.

2 ALGORITHMS AND METHODS

2.1 X-ray transport and absorption

In previous works using the SILCC simulation framework (Walch et al. 2015; Girichidis et al. 2016; Gatto et al. 2017; Peters et al. 2017) the X-ray flux was assumed to be constant and was simply scaled with the background interstellar UV radiation field (ISRF). Here, we develop a fully self-consistent X-ray absorption module and introduce the algorithms used for X-ray radiative transfer and absorption. We split the X-ray radiation field into N_E energy bins, equally spaced in log E, and calculate a mean cross-section for each bin, $\langle \sigma_i \rangle$. 1D radiative transfer is very simple and requires little explanation. For 3D simulations in this paper we consider only an isotropic external radiation field to study the effects of X-rays on the chemistry of molecular clouds, similar to assuming an isotropic background interstellar UV radiation field (e.g. Draine 1978). We use the TREERAY/OPTICAL DEPTH algorithm (Wünsch et al. 2018) for 3D radiative transfer, implemented in the FLASH code (Fryxell et al. 2000), described in more detail below. Modifying TREERAY/OPTICAL DEPTH to handle anisotropic radiation fields is a relatively simple extension.

The term 'flux' can mean different things depending on context: when we say X-ray flux, denoted F_X, we mean (i) uni-directional energy flux of radiation for 1D slab-symmetric calculations, and (ii) $4\pi J_X$ (where J_X is the angle-averaged mean intensity) for 3D

simulations. In both cases it is the X-ray energy flux available to be absorbed at a point. We integrate over a given energy range, usually 0.1–10 keV, and so the units are (erg cm^{-2} s^{-1}). In the nomenclature of Röllig et al. (2007), the 1D simulations have uni-directional flux, and the 3D simulations isotropic flux. We also quote the X-ray energy density, $E_{\rm rad}$, for clarity and for ease of comparison with other potentially relevant energy densities, such as CRs, FUV radiation, thermal energy, etc. For the 1D flux, $E_{\rm rad} = F_X/c$ (c is the speed of light), and for 3D calculations $E_{\rm rad} = 4\pi J_X/c$.

2.1.1 X-ray absorption cross-section

X-rays are mainly absorbed by ions of heavy elements (especially iron) because their large cross-section more than makes up for their trace abundance. However, calculating the absorption by each ion individually is computationally expensive, as it requires knowledge of the abundance and ionization stage of many heavy ions and is therefore only feasible for detailed PDR/XDR codes (e.g. Meijerink & Spaans 2005; Ferland et al. 2013). Panoglou et al. (2012) used a mean cross-section that takes account of all of the heavy elements in a single analytic function, which we also use:

$$\sigma_{\rm x} = 2.27 \times 10^{-22} E_\gamma^{-2.485} \ {\rm cm}^2 \tag{1}$$

per H nucleus, where E_γ is the photon energy in keV.

This cross-section was also used by Shang et al. (2002) and is based approximately on results of Morrison & McCammon (1983) for a gas of solar metallicity with abundances in table 1 of this paper (typically within 0.1 dex of updated values from Asplund et al. 2009). It assumes that the temperature is low enough that heavy atoms are not significantly ionized, and so the dominant absorbers at large energy are those heavy atoms with K and L shells and corresponding large cross-sections. The approximate formula does not capture resonances or sharp jumps in cross-section at K or L shell edges (e.g. de Avillez & Breitschwerdt 2012a). Morrison & McCammon (1983) and Wilms, Allen & McCray (2000) show that H and He contribute significantly to the cross-section up to the oxygen K-shell edge at $\sim$0.5 keV, and that a power law with slope ~ -2.5 is a good approximation to the total cross-section in the range 0.1−10 keV. Our cross-section is therefore reliable as long as the electron fraction is small, and fails first at low energies ($\lesssim$0.5 keV) as the ionization fraction increases. For highly ionized gas the approximate cross-section becomes unreliable and a more accurate treatment would be required, but our aim here is to model molecular clouds and so this regime is not relevant. The cross-section is only valid at or near solar metallicity and does not scale simply with metallicity because H and He contribute significantly for $E_\gamma \lesssim 0.5$ keV. Morrison & McCammon (1983) show that the cross-section shows only marginal changes even when most heavy elements are completely depleted on to grains.

For an energy bin, i, in the energy range $E_a < E_\gamma < E_b$, with $E_m = 0.5(E_a + E_b)$, and defining $\sigma_m \equiv \sigma_x(E_m)$, we define the mean cross-section $\langle \sigma_i \rangle$ using the relation

$$\exp\left(-\frac{\langle\sigma_i\rangle}{\sigma_m}\right) = \frac{1}{E_b - E_a}\int_{E_a}^{E_b} \exp\left(-\frac{\sigma_{\rm x}(E)}{\sigma_m}\right) dE. \tag{2}$$

This formula averages the attenuation factor over the energy bin, and this is used to obtain an appropriate $\langle \sigma_i \rangle$. This provides a better estimate of the energy absorbed than using a simple average of σ_x. The constant σ_m is chosen so that the exponent is of order unity over most of the integral, but in principle a different value could be used. A similar averaging was used by Mackey & Lim (2010) to improve photon (and hence energy) conservation in photoionization calculations.

We stress that computational requirements force us to minimize the number of bins, N_E, and so it is always the case that σ_x changes significantly within the energy bin because of its strong scaling with energy. There is no way to avoid some level of inaccuracy when choosing $\langle \sigma_i \rangle$ without making assumptions about the shape of the X-ray spectrum.

2.1.2 One-dimensional radiative transfer

For uni-directional flux the equation of radiative transfer is very simple, having a source at infinity with flux entering the simulation domain, $F_{X,0}$, and only absorption everywhere else (i.e. scatterings are not considered). For an energy bin i, the X-ray flux, $F_{X,i}$, at a point x is simply

$$F_{X,i}(x) = F_{X,0} \exp\left\{-\tau_i(x)\right\}, \tag{3}$$

where $\tau_i(x) \equiv \int_{-\infty}^{x} n_{\rm H}(x')\langle\sigma_i\rangle {\rm d}x'$ is the optical depth along the ray to point x, and $n_{\rm H}$ is the local number density of H nuclei.

2.1.3 Three-dimensional radiative transfer

In the 3D FLASH simulations we use the TREERAY/OPTICAL DEPTH algorithm (Wünsch et al. 2018), which is similar to the TREECOL method developed by Clark, Glover & Klessen (2012). The TREERAY/OPTICAL DEPTH algorithm computes the mean column density of any given species in every time-step and for each cell of the computational domain using a HEALPIX tessellation (Górski et al. 2005) with $N_{\rm pix}$ pixels for each grid cell, using an Oct-tree method. We modified the tree solver such that it can be used to calculate the X-ray optical depth between each grid cell and the boundary of the computational domain. As a result, we obtain the columns and fluxes for every grid cell. Here we use $N_{\rm pix} = 48$ and a geometric opening angle criterion (Barnes & Hut 1986) with an opening angle of $\theta_{\rm lim} = 0.5$.

We consider that the simulation domain is embedded in a uniform and isotropic external X-ray radiation field with mean intensity J_ν, where ν is frequency. For an isotropic 3D radiation field the intensity, I_ν, is equal to J_ν, and so all rays entering the simulation domain satisfy this equality. For an X-ray energy bin, denoted i, the external mean intensity can be denoted $J_{0,i}$, and the fluxes $F_{0,i} \equiv 4\pi J_{0,i}$ are input parameters to our calculations.

The intensity along a ray, labelled n, from the edge of the simulation domain to a grid cell located at $\mathbf{r}$ can be obtained by solving the equation of radiative transfer with zero emissivity, as in the 1D case above:

$$I^n_{X,i}(\mathbf{r}) = J_{0,i} \exp\left(-\tau_i^n\right), \tag{4}$$

where $\tau_i^n \equiv \int n_{\rm H}(\mathbf{r}')\langle\sigma_i\rangle {\rm d}\mathbf{r}'$ is now the optical depth along the ray. For a given number of rays, N, uniformly covering 4π steradians, the mean intensity at r is simply the average value of $I^n_{X,i}(\mathbf{r})$:

$$J_{X,i}(\mathbf{r}) = \frac{1}{N}\sum_{n=1}^{N} I^n_{X,i}(\mathbf{r}) = \frac{J_{0,i}}{N}\sum_{n=1}^{N} \exp\left(-\tau_i^n\right) \tag{5}$$

The local attenuated flux at $\mathbf{r}$ is then

$$F_{X,i}(\mathbf{r}) \equiv 4\pi J_{X,i}(\mathbf{r}) = \frac{F_{0,i}}{N}\sum_{n=1}^{N} \exp\left(-\tau_i^n\right). \tag{6}$$

From this we can calculate a local rate of X-ray energy absorption, $H_{\rm x}$ (erg s^{-1}) per H nucleus using

$$H_{\rm x} = \sum_{i=1}^{N_E} F_{X,i} \langle \sigma_i \rangle, \quad (7)$$

where the sum is over all energy bins.

We use isolated boundary conditions for the OPTICAL DEPTH module, which means that the simulation domain is bathed in a uniform and isotropic (but potentially time-varying) X-ray radiation field. The X-ray optical depths are calculated between the target cell and the boundary of the simulation domain, so that every cell contributes to attenuating the radiation field seen at a given point. Such a set-up is not always appropriate for X-ray radiation fields, which are often dominated by point sources (e.g. Ponti et al. 2015), but it is an improvement on a 1D slab (see Section 3.1) because it allows us to consider a more realistic density field. We also run our calculations in the limit of infinite speed of light.

The column densities of total gas, CO, and H_2 are necessary to compute the (self-) shielding of gas from the ISRF, whereas the X-ray attenuation factors, $\exp(-\tau_i^n)$, depend only on the total gas column density. We therefore calculate the attenuated X-ray flux for each of the N_E X-ray energy bins arriving at every cell using equation (6) and use it as an input for the chemical network. The radiative transfer is completed before the chemistry update in FLASH, and so we need to store the attenuation factors

$$\frac{1}{N} \sum_{n=1}^{N} \exp(-\tau_i^n) \quad (8)$$

for each X-ray energy bin, i, at every grid cell. This is accomplished by adding N_E scalar fields to the grid. Within the chemistry network, the local X-ray absorption rate is calculated using equation (7).

2.2 Chemical network

We use a chemical network based largely on the NL99 network of Glover & Clark (2012), which combines a model for hydrogen chemistry taken from Glover & Mac Low (2007a,b) and a model for CO chemistry introduced by Nelson & Langer (1999). We also include a number of modifications and updated reaction rates as suggested by more recent work (e.g. Gong et al. 2017). The X-ray reactions and rates are taken largely from Yan (1997) and Meijerink & Spaans (2005; hereafter MS05).

The number fraction of species Q with respect to the total number of hydrogen nuclei is denoted y(Q), and $Y_{\rm R}$ is the fractional abundance by number of nuclei of *element* R with respect to hydrogen. For example, $y(\rm H_2) \in [0, 0.5]$ because $Y_{\rm H} \equiv 1$, and y(CO) $\in [0, \min(Y_{\rm C}, Y_{\rm O})]$. Note in particular that the electron fraction, $y(\rm e^-)$, can be larger than unity with this definition.

The chemical species that we solve for are listed in Table 1. The non-equilibrium species solved for are H_2, H^+, CO, C^+, CH_x, OH_x, HCO^+, He^+, and M^+. Following Nelson & Langer (1999), CH_x is a proxy species for simple hydrocarbons CH, CH_2, CH_3, etc., and similarly OH_x for OH, H_2O, etc. Intermediate molecular ions CH^+, $CH2^+$, OH^+, etc., are also included in CH_x and OH_x, as appropriate, as well as the neutral species. We assume that each CH_x and OH_x molecule only contains one H atom for accounting purposes, but this makes no difference because the abundance of the species is very low compared to hydrogen.

M is a proxy element for metals (e.g. N, Mg, Si, S, Fe) that can be the primary source of electrons in molecular gas at large column density. We assume that M is a two-ionization-stage atom, tracking M^+ as a species, and neutral M with a conservation equation. The abundances of neutral atomic species H, He, C, are also computed using conservation equations, and we assume that the abundance of doubly (and more highly) ionized species is negligible. Oxygen is also treated as a two-ionization-stage atom, and its ionization fraction is assumed to be the equilibrium value (after accounting for the fraction of O that is in OH_x and CO) because of the rapid charge exchange reactions with H and H^+ (Stancil et al. 1999). The equilibrium abundance of H_3^+ is calculated from the local chemical abundances and temperature, and used in the network following Nelson & Langer (1999). In total there are nine species in the network that are solved by the ODE solver (Brown, Byrne & Hindmarsh 1989), five species tracked by conservation equations (H, He, C, M, e^-) and four species (O, O^+, H_2^+, H_3^+) tracked by assuming equilibrium abundances or instantaneous further reaction. All of these contribute to gas heating and cooling.

Table 1. Species calculated in our chemical network.

Species	Treatment
H	Conservation equation
H^+	ODE solve
H_2	ODE solve
OH_x	ODE solve
C	Conservation equation
C^+	ODE solve
CO	ODE solve
CH_x	ODE solve
HCO^+	ODE solve
He	Conservation equation
He^+	ODE solve
M	Conservation equation
M^+	ODE solve
O	Equilibrium
O^+	Equilibrium
H_2^+	Instantly reacts further
H_3^+	Equilibrium
e^-	Conservation equation

Table 2. Elemental abundances in the gas phase by number with respect to hydrogen nuclei, $Y_{\rm R}$.

Species	$Y_{\rm R}$
H	1.0
He	0.1
C	1.4×10^{-4}
O	3.4×10^{-4}
M	1.0×10^{-5}

The elemental abundances are listed in Table 2. The metal abundance can be set somewhat arbitrarily because it covers a number of different elements, although we take reaction rates appropriate for silicon throughout the paper. Maloney et al. (1996) considered Si, Fe, S, and Ni, with the most abundant being Si (3.5×10^{-6}) and S (1.0×10^{-5}). Nelson & Langer (1999) used a rather low value of $Y_{\rm M} = 2 \times 10^{-7}$, whereas Bisbas et al. (2015) use $Y_{\rm M} = 4 \times 10^{-5}$ as the sum of the abundances of all relevant gas-phase metal abundances, and Gong et al. (2017) used Si as a proxy for all metals with $Y_{\rm Si} = 1.7 \times 10^{-6}$. The metal abundance is important at high column densities because it determines the electron fraction once C^+ has recombined.

The collisional reactions are listed in Table A1, and photoreactions in Table A2 in Appendix A. An analysis of the differences

between results with and without the Gong et al. (2017) additional reactions is also presented in Appendix A. A noteworthy addition is that we follow Gong et al. (2017) in including grain recombination reactions for C^+, He^+, M^+, as well as H^+. In addition, in view of the potential importance of He^+ ions in the CO chemistry of X-ray-irradiated gas, it is worthwhile highlighting the difference in our treatment of He^+ recombination. Gong et al. (2017) use the case B radiative recombination rate from Hummer & Storey (1998), while we attempt to account for the fact that in gas that is optically thick to ionizing photons, the actual radiative recombination rate lies between the case A and case B rates owing to absorption of helium recombination photons by atomic hydrogen (Osterbrock 1989). In addition, we also account for dielectronic recombination of He^+, a process neglected by Gong et al. (2017). At low temperatures, this process is unimportant, but in hot gas ($T \sim 10^5$ K), it comes to dominate the total He^+ recombination rate.

2.2.1 H_2^+ and H_3^+ abundance and reactions

There are four formation channels for H_2^+: CR ionization of H_2 (#56 in Table A2), charge exchange between He^+ and H_2 (#27 in Table A1), charge exchange between H_2 and H^+ (#18 in Table A1), and X-ray ionization of H_2 (#66 in Table A2). H_2^+ is considered to react immediately once it is formed and, following the discussion in MS05, it has three further reaction pathways:

(i) dissociative recombination with an electron to 2H plus 10.9 eV of heat (#43 in Table A1);
(ii) charge exchange with H to produce H_2 and H^+ and 0.94 eV of heating (#17 in Table A1); and
(iii) further reaction with H_2 to produce H_3^+ and H (with subsequent recombination or reaction with other species), with net heating of 8.6 eV per H_3^+ ion production (#32 in Table A1).

The creation rate of these products is given by the H_2^+ formation rate multiplied by the fraction of the H_2^+ ions that follow each pathway. H_2^+ can also be photodissociated by the interstellar radiation field, but this process is competitive with processes (ii) and (iii) above only when $n/G_0 < 1$ (Glover 2003). Since $n/G_0 \gg 1$ in typical molecular cloud conditions, we are justified in neglecting this process in the models presented in this paper.

We assume that H_3^+ has its equilibrium abundance at all times. Its only significant creation channel[1] is through H_2^+ (#32 in Table A1), and it is destroyed by

(i) reaction with C to form CH_x (#21 in Table A1)
(ii) reaction with O to form OH_x (#22 in Table A1), and further with an electron to produce O + 3H (#23 in Table A1);
(iii) reaction with CO to form HCO^+ and H_2 (#24 in Table A1);
(iv) dissociative recombination with an electron (#20 in Table A1); and
(v) charge exchange with M to form H_2 + H + M^+ (#19 in Table A1).

The equilibrium abundance is obtained by balancing the creation rate with the destruction rates listed.

[1] H_3^+ can also form via the radiative association of H_2 with H^+, but this process is slow (see e.g. the discussion in Glover & Savin 2009), and is only competitive with formation via H_2^+ in gas with a very low H_2 abundance. In these conditions, the H_3^+ abundance itself is very small and H_3^+ plays a negligible role in the gas chemistry.

2.3 X-ray heating, ionization, and dissociation

X-rays are absorbed by dust and gas, affecting both components through the following processes, most of which we include. They are described in more detail below:

(i) Dust heating, following Yan (1997).
(ii) Dust destruction and charging by X-rays.
(iii) Direct ionization of an atom/molecule by X-rays. This is generally only important for elements that have a K-shell, because these elements have much larger direct ionization cross-sections than lighter elements. For H, H_2, and He it is negligible (e.g. Dalgarno, Yan & Liu 1999).
(iv) Secondary ionization of atoms/molecules through collisions with the fast (keV) electrons that are produced by a direct X-ray ionization. This is the main ionization channel for H, H_2, and He.
(v) Secondary ionization/dissociation of atoms/molecules through FUV radiation that is locally generated by H_2 molecules, which are collisionally excited by fast electrons. This provides important photodissociation channels for molecules (except H_2) and photoionization channels for atomic species with low-ionization energy (e.g. C).
(vi) Coulomb heating of the gas arising from energy exchange between the fast electrons and other charged particles in the gas.
(vii) Heating through dissociation of molecules and ionization of atoms (these rates are typically already in the chemical model, and the X-rays only increase the heating rate).

For the dust we consider only heating (i), ignoring ionization and dust destruction (ii). This is reasonable for the molecular clouds that we consider, but would not be suitable for strongly irradiated, hot gas. We also do not consider direct ionization/dissociation by X-rays (iii), but only secondary ionizations through collisional (iv) and FUV (v) processes. All of the other processes are included as described below.

2.3.1 Dust heating

The dust temperature, T_D, in an X-ray irradiated gas is calculated following Yan (1997) and MS05 as

$$T_D = 1.5 \times 10^2 \left(\frac{H_x}{10^{-18}\ \mathrm{erg\ s^{-1}}} \right)^{0.2} \mathrm{K}. \quad (9)$$

We take the maximum of this temperature and the radiative equilibrium temperature resulting from FUV irradiation (which is calculated following Glover & Clark 2012). There is an evidence for dust temperatures between 125 and 150 K in the circumnuclear disc of the Galactic Centre via detection of the $J = 4 - 3$, $v_2 = 1$ vibrationally excited transition of HCN, which Mills et al. (2013) argue is excited by local IR radiation from hot dust grains. In our 3D simulations described later the dust temperature ranges from 10 to 70 K.

2.3.2 Coulomb heating

Secondary electrons are produced when an X-ray photon is absorbed by a heavy element, resulting in ionization and the ejection of an electron with kinetic energy comparable to the photon energy. The absorbed X-ray power per H nucleus, H_x (erg s^{-1}), is transferred to these hot electrons, and subsequently goes partly into heating the gas and partly into ionizations (Dalgarno et al. 1999). The fraction that goes into heating is determined in part by the electron abundance in the gas, because the heating arises from energy exchange through

Coulomb interactions between the hot electron and the thermal electrons (and, to a lesser extent, thermal ions). For small electron fractions, most of the X-ray energy goes into ionizations, but the heating fraction increases towards unity as the electron fraction increases (Dalgarno et al. 1999). The heating fraction is also dependent on the energy of the hot electron (and hence the energy of the X-ray photon), because higher energy electrons are much more likely to cause ionizations in a collisional interaction than lower energy electrons. We follow MS05 in implementing the results of Yan (1997) and Dalgarno et al. (1999) to model these processes.

The Coulomb heating rate by secondary electrons is obtained from the tables of Dalgarno et al. (1999) using the local abundances of electrons, H, and H_2. The local heating rate, Γ_x (erg cm^{-3} s^{-1}) is given by

$$\Gamma_{\rm x} = \eta n_{\rm H} H_{\rm x}, \tag{10}$$

where η is a heating efficiency obtained from tables in Dalgarno et al. (1999). The efficiency depends on $y(e^-)$, $y(H)$, $y(H_2)$, and $y(He)$.

Coulomb heating becomes more efficient as $y(e^-)$ increases, and the fit of Dalgarno et al. (1999) becomes invalid for $y(e^-) > 0.1$. We therefore assume that, for $y(e^-) > 0.1$, the fraction of absorbed X-ray energy that goes to Coulomb heating, η, scales linearly with the electron fraction, starting from the Dalgarno et al. (1999) value at $y(e^-) = 0.1$ and reaching 100 per cent for $y(e^-) \geq 1$, i.e.

$$\eta[y(e^-)] = \eta(0.1) + \frac{1-\eta(0.1)}{0.9}\left(\min[1, y(e^-)] - 0.1\right), \tag{11}$$

where the minimum operator ensures $\eta \leq 1$ even when $y(e^-) > 1$. This interpolation is important for ensuring that the ODE solver converges in highly ionized gas.

2.3.3 *Secondary collisional ionization*

The hot electrons ionize and dissociate, as well as heat, the gas. H is ionized with rate $\zeta(H)$ per H atom per second, and He with rate $\zeta(He)$ per He atom per second. Molecular hydrogen, H_2, is dissociated (with rate $\zeta_D(H_2)$ per H_2 molecule per second) or ionized to H_2^+ (with rate $\zeta(H_2)$ per H_2 molecule per second).

These collisional ionization and dissociation rates by secondary electrons are calculated by interpolating the tables of Dalgarno et al. (1999) for $y(e^-) \leq 0.1$. As for the heating rates above, for $y(e^-) > 0.1$ we take the Dalgarno et al. (1999) rates at $y(e^-) = 0.1$ and make them proportional to the abundance of the neutral species being ionized (or dissociated) so that the rate has the correct limit as full ionization is approached, e.g.

$$\zeta(H)y(H) = \frac{H_{\rm x}}{W_{\rm H}(y(e^-)=0.1)} y(H)^{1-(0.1/y(e^-))^3}. \tag{12}$$

Here $W_{\rm H}$ is the mean energy per H ionization from Dalgarno et al. (1999). This is an ad hoc extrapolation of the Dalgarno et al. (1999) tables but is not important for the results presented in this work because we are not studying highly ionized plasmas. It does, however, ensure that the ODE solver converges for all values of $y(e^-)$. The rates for reactions #62, #63, #66, and #67 from Table A2 are calculated using this formula and the tables from Dalgarno et al. (1999).

C is ionized by secondary electrons, with a rate 3.92 times that of H according to appendix D3.2 of MS05. We generalize their equation to the following:

$$\zeta(C)y(C) = \frac{\zeta(H)y(H) + \zeta(H_2)y(H_2)}{y(H) + y(H_2)} 3.92 y(C). \tag{13}$$

This has the correct limiting values when H is fully atomic and fully molecular, and is the equation used for reactions #64, #65, #68–71 in Table A2. Similarly CO, CH_x, OH_x, HCO^+ can be collisionally ionized and destroyed by secondary electrons. For CO, CH_x, and HCO^+ we use the same scaling factor as for C (3.92), whereas for OH_x we use a scaling factor of 2.97 appropriate for oxygen (MS05). For M, we use the same scaling factor as for silicon, 6.67. For simplicity we assume that ionization of all the carbon-bearing molecules produces C^+, OH_x produces O and H^+, and HCO^+ produce C^+ and H^+ and O. Ionization of M produces M^+.

These factors of 3.92 for C, 2.97 for O, and 6.67 for Si were obtained by integrating the cross-sections over the range 0.1−10 keV to obtain an average value (see MS05), whereas in reality they should vary as a function of energy bin. In all of our calculations, however, these reactions are negligible compared with dissociation by the locally generated FUV field and so such an approximate treatment can be accepted. For future work that consistently includes the transition to highly ionized plasmas one would need to improve this aspect of our chemical model (cf. de Avillez & Breitschwerdt 2012b), ideally considering the energy-dependent cross-section of each ion.

2.3.4 *Secondary ionization by locally generated FUV radiation*

A local FUV radiation field is generated by collisional excitation of H_2 and H by hot electrons (Prasad & Tarafdar 1983; Gredel, Lepp & Dalgarno 1987; Maloney et al. 1996). In our network, this contributes to the ionization of C and M (rates from Maloney et al. 1996; Yan 1997), and to the dissociation of CH_x, OH_x, HCO^+, and CO (Yan 1997).

The Gredel et al. (1987) rate for CO destruction per second is fitted with

$$R_{\rm CO}^{\rm FUV} y({\rm CO}) = 2.7\sqrt{y({\rm CO})\frac{T}{10^3\,{\rm K}}}\,\zeta(H_2)y(H_2), \tag{14}$$

and this is often used (e.g. Maloney et al. 1996, MS05). This does not scale linearly with $y(CO)$ as $y(CO) \rightarrow 0$, which causes numerical problems for the ODE solver (the destruction time-scale goes to zero as $y(CO) \rightarrow 0$). The physical reason for this scaling is that the process is photon limited: photons are produced at a rate that depends on $\zeta(H_2)$ and $n(H_2)$, and are then primarily absorbed by CO.

We instead use the UMIST12 (McElroy et al. 2013) rate for reaction #74 in Table A2 because it has a more numerically stable asymptotic behaviour, although it may be less accurate for $T > 50$ K than the Maloney et al. (1996) rate (T. Millar, private communication), and it probably underestimates the rate at which CO is destroyed as the CO abundance goes to zero:

$$R_{\rm CO}^{\rm FUV} y({\rm CO}) = 210.0\left(\frac{T}{300\,{\rm K}}\right)^{1.17} y({\rm CO})\zeta(H_2)y(H_2). \tag{15}$$

For other species we follow previous authors (Maloney et al. 1996; Yan 1997, MS05) using the following functional form for reactions #72, #73, #75, and #76 in Table A2:

$$R_{\rm x}^{\rm FUV} y({\rm x}) = [p_{\rm m}\zeta(H_2)y(H_2) + p_{\rm a}\zeta(H)y(H)]\,\frac{y({\rm x})}{1-w}, \tag{16}$$

where $p_{\rm m}$ relates to the cross-section of species x for dissociation/ionization by Lyman–Werner photons, and $p_{\rm a}$ by Lyman α photons. The values of $p_{\rm m}$ and $p_{\rm a}$ used are given in Table 3. The grain albedo, w, is taken to be 0.5 for all energies (Maloney et al. 1996; Panoglou et al. 2012). CRs also produce secondary electrons

Table 3. Constants for destruction of species by FUV radiation generated by hot electrons exciting molecular (p_m) and atomic (p_a) hydrogen (see equation 15). Values for OH and CH are used for OH_x and CH_x, respectively, and values for Si are used for M. Values for p_a are already multiplied by $\epsilon_L = 0.1$, following Lepp & Dalgarno (1996). Most p_m values are taken from the UMIST12 data base (McElroy et al. 2013) and are multiplied by 2 because they are relative to a CR/X-ray ionization rate per H_2 molecule, whereas we use an ionization rate per H nucleus. The p_m value for M is attributed to Rawlings (1992, private communication) in McElroy et al. (2013). In the fourth column, the first reference is for p_m and the second for p_a. References: 1 Gredel et al. (1987); 2 McElroy et al. (2013); 3 Lepp & Dalgarno (1996); 4 Yan (1997); 5 Maloney et al. (1996); 6 Gredel et al. (1989).

Species	p_m	p_a	References
C	510	0	1,5
M	4230	10 500	2,4
OH_x	508	87.6	6,3
CH_x	730	35	6,4

and a local FUV field in the same way, and so reactions #59, #60, and #61 have the same form.

Heays, Bosman & van Dishoeck (2017) have recently calculated updated rate coefficients for p_m (their table 20). Their new values are similar to what we use here. In particular their updated value for C is 520 (scaled to our normalization) compared with our value of 510. This and the CO rate (equation 15), for which Heays et al. (2017) refer to Gredel et al. (1987), are the key ones for our work. For the others, the rate for M is so large that it remains ionized to the largest column densities considered, and our treatment of CH_x and OH_x is very approximate and so a factor of $\sim$2 difference in p_m does not impact on our results.

2.4 Time-dependent solution in the FLASH code

Chemistry and cooling are operator split from the other parts of the FLASH code (Fryxell et al. 2000), which compute e.g. the magneto-hydrodynamic evolution of the gas or the gas self-gravity. As in Walch et al. (2015), the chemistry and gas temperature are integrated simultaneously using the ODE solver DVODE (Brown et al. 1989). We employ sub-timestepping if the chemical abundances or the internal energy are about to change significantly in a given cell. This ensures that the reaction and cooling rates are accurate even if the gas temperature changes by a large factor over a single time-step. The heating and cooling processes considered and a table of references for their implementation are given in Appendix B.

The inputs to the ODE solver and the chemical network are the total column density N_H, the column densities of CO and H_2, the attenuated ISRF, the attenuated X-ray flux in each energy bin (see Section 2.1), the gas density, internal energy, and the chemical state at the beginning of a time-step. The ODE solver integrates the equations and returns the updated internal energy and chemical state at the end of each time-step.

Therefore, chemistry and thermodynamics are mostly time dependent, giving us an advantage over previous XDR calculations because we can study what happens when the X-ray radiation field varies on time-scales shorter than the chemical or thermal time-scale in full 3D geometry. There are some caveats to this statement: we do use a chemical network in which we assume (i) that the O/O^+ ratio has reached its equilibrium value based on the H^+ fraction; (ii) that H_2^+ reacts instantly to produce further products; and (iii) that H_3^+ has its equilibrium abundance; and (iv) that the locally generated UV radiation field is produced instantly by hot electrons in the molecular cloud. The first three approximations are made because these reactions are usually faster than others which are calculated in a fully time-dependent way. Regarding the fourth assumption, we note that the time-scale on which the local UV field builds up is of the order of the stopping time of the hot photoelectrons (i.e. the time it takes for them to lose the bulk of their kinetic energy). At typical molecular cloud densities this is $\ll$1 yr (Dalgarno et al. 1999), much shorter than the time-scales of interest in Section 5 and, therefore, for our purposes the approximation that the UV field appears instantly is reasonable.

Table 4. Simulation parameters for the four test problems of MS05.

Model	n_H (cm^{-3})	F_X (erg cm^{-2} s^{-1})	E_{rad} (erg cm^{-3})
1	10^3	1.6	5.34×10^{-11}
2	10^3	160	5.34×10^{-9}
3	$10^{5.5}$	1.6	5.34×10^{-11}
4	$10^{5.5}$	160	5.34×10^{-9}

3 TEST PROBLEMS

Our chemical network is much smaller than networks used by XDR calculations in the literature that assumed chemical equilibrium (e.g. Meijerink & Spaans 2005; hereafter MS05). This means that we have fewer potential coolants in the gas and fewer potential sources of electrons in highly shielded gas, although the inclusion of species M is intended to mimic the effects of a number of metals that are not explicitly incorporated. Furthermore, in some cases we are using different reaction rates and cooling rates from previous authors. These differences may be significant, so it is important to benchmark our results against other codes, and try to understand any differences that may be present. We begin by considering the test problems studied by MS05, and then run calculations using a large range of densities and X-ray fluxes, to make sure that our model produces sensible results for all ISM conditions.

3.1 Comparison with MS05

We consider the four calculations by MS05 as test problems for our XDR chemistry module, and follow these authors by referring to them as models 1–4. They are 1D XDR calculations of an infinite slab that is irradiated from one side by X-ray radiation, and follow closely the work of Yan (1997). The gas density and X-ray fluxes for models 1–4 are given in Table 4. Models 1 and 2 have $n_H = 10^3$ cm^{-3} whereas models 3 and 4 have a density about 300 times larger. Models 1 and 3 have a moderate total X-ray flux of $F_X = 1.6$ erg cm^{-2} s^{-1}, and models 2 and 4 have a flux 100 times larger. MS05 considered an X-ray spectrum of the form $F \propto \exp(-E/10\,\mathrm{keV})$ (a typo in MS05 said 1 keV in the exponential instead of 10 keV; R. Meijerink, private communication), and they only considered X-rays in the range 1–10 keV. We run the calculations with 10 energy bins, logarithmically spaced between 1 and 10 keV, shown in Table 5. The ISRF is set to $G_0 = 10^{-6}$, i.e. effectively no UV irradiation. This radiation field is plotted in Fig. 1 together with the absorption cross-section used in each of the 10 bins. For consistency with previous work, the radiation field is assumed to be zero from the Lyman limit up to 1 keV. This can be justified because of the large interstellar absorption cross-section at these energies, although the abrupt switch-on of the X-rays at 1 keV is somewhat artificial.

We set-up a 1D grid with 200 logarithmically spaced grid-zones, without hydrodynamics and with constant gas density, and we set

Table 5. Energy bins, mean absorption cross-section, X-ray flux, and energy density in each bin for MS05 test models 1 and 3. Models 2 and 4 are identical except that the flux in each bin is multiplied by 100. Bin energy limits $E_{\rm min}$ and $E_{\rm max}$ are in keV, mean cross-section $\langle\sigma_i\rangle$ in cm^{-2}, flux F_X is in erg cm^{-2} s^{-1} per bin, and energy density $E_{\rm rad}$ in units 10^{-12} erg cm^{-3} per bin.

Bin, i	$E_{\rm min,\,i}$	$E_{\rm max,\,i}$	$\langle\sigma_i\rangle$	$F_{X,\,i}$	$E_{\rm rad,\,i}$
0	1.000	1.259	1.686×10^{-22}	0.069	2.30
1	1.259	1.585	9.515×10^{-23}	0.084	2.81
2	1.585	1.995	5.369×10^{-23}	0.102	3.41
3	1.995	2.512	3.030×10^{-23}	0.123	4.10
4	2.512	3.162	1.710×10^{-23}	0.146	4.87
5	3.162	3.981	9.648×10^{-24}	0.171	5.69
6	3.981	5.012	5.444×10^{-24}	0.196	6.54
7	5.012	6.310	3.072×10^{-24}	0.220	7.33
8	6.310	7.943	1.734×10^{-24}	0.239	7.97
9	7.943	10.00	9.782×10^{-25}	0.250	8.35

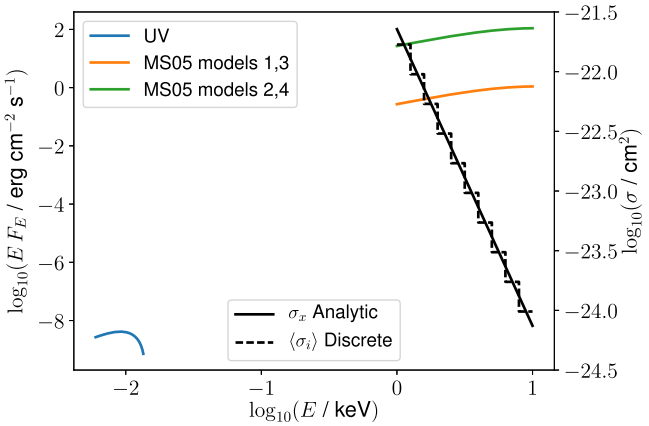

Figure 1. UV flux (blue) and X-ray flux from Table 5 for the four test problems considered by MS05 in Section 3.1 (left y-axis) and X-ray absorption cross-section (right y-axis). E is the energy in keV and F_E is the energy flux in units erg cm^{-2} s^{-1} keV^{-1}. For the cross-section, the continuous black line plots equation (1) from Panoglou et al. (2012), and the dashed black line the discrete cross-section used for each of the 10 energy bins. For these tests the UV flux is scaled to $G_0 = 10^{-6}$ to make it insignificant.

the grid-zones so that column densities from $N_{\rm H} = 10^{16}$ cm^{-2} to 10^{26} cm^{-2} are calculated. The initial conditions are uniform, with sound speed 10 km s^{-1}, and partially ionized with $y({\rm H}^+) = 0.5$, $y({\rm He}^+) = 0.05$, $y({\rm C}^+) = Y_{\rm C}$, $y({\rm M}^+) = Y_{\rm M}$, and molecular species set to have abundance 10^{-20}. The column density of H, H_2, and CO are trivially calculated at each time-step on such a grid, and these are used as an input to the chemistry solver. The chemical and thermodynamic properties are then integrated for each grid point over a time-step. The initial time-step is 10^5 s, and this is doubled after each step. The MS05 calculations assume chemical and thermal equilibrium, so we integrate our chemical network for 10^9 yr to ensure that equilibrium conditions are obtained in all cases. Models 1 and 2 reach equilibrium in 5–10 Myr, and models 3 and 4 take <1 Myr because of their higher gas density.

The results obtained at the end of the integration are shown in Fig. 2. The effects of attenuation are negligible for $N_{\rm H} \lesssim 10^{21}$ cm^{-2} (which corresponds to a visual extinction $A_{\rm V} \sim 0.5$), and attenuation is basically complete by $N_{\rm H} \gtrsim 10^{25}$ cm^{-2}; the abundances and temperature tend to constant values in these limits. Models 1 and 2 have a moderate gas density ($n_{\rm H} = 10^3$ cm^{-3}) and so weaker gas cooling (per unit volume) than the denser models 3 and 4. As a result they have higher equilibrium temperatures at all $N_{\rm H}$. At low $N_{\rm H}$, model 1 has $T \approx 10^3$ K, model 2 has $T \approx 10^4$ K, model 3 has $T \approx 10^2$ K, and model 4 has $T \approx 10^{3.6}$ K. All models are charaterized by decreasing temperature and electron fraction in the range $N_{\rm H} \in [10^{22}, 10^{25}]$ cm^{-2}. Models 1, 2, and 4 have low molecular fractions at low column density, and increasing abundance with increasing column density. Model 3 is so dense that the moderate X-ray flux cannot destroy the molecules even at low column density, and so it is mostly molecular at all column densities. For all four calculations, the atomic-to-molecular transition happens at $T \sim 100$ K and when $y({\rm e}^-) \lesssim 10^{-4}$, although the column density at which this occurs is strongly dependent on gas density and X-ray flux. The C to CO transition occurs at approximately the same column density as the H to H_2 transition.

Our results can be directly compared with figs 3 and 4 of MS05. Taking each model in turn, we discuss the similarities and differences between our results and those of MS05.

3.1.1 *Model 1 (Fig. 2, top-left panel)*

At small $N_{\rm H}$ we find larger $y(H_2)$, larger $y({\rm C}^+)$, smaller T, and $y({\rm e}^-)$ than found by MS05. At large $N_{\rm H}$ we cannot see the asymptotic values that the MS05 results will tend to, but the results appear comparable. At intermediate $N_{\rm H}$ some changes occur at smaller $N_{\rm H}$ in our calculations: the H to H_2 transition occurs at $N_{\rm H} \sim 10^{23.7}$ cm^{-2}, at which point $T < 100$ K, $y({\rm e}^-) \sim 10^{-4.5}$. These T and $y({\rm e}^-)$ values are consistent with MS05, except that they find the transition at $N_{\rm H} \sim 10^{24.2}$ cm^{-2}, about 0.5 dex larger than us. MS05 also find that $y({\rm C}^+)$ remains large until $N_{\rm H} \sim 10^{24.2}$ cm^{-2}, whereas we find a significant decrease already at $N_{\rm H} \sim 10^{23}$ cm^{-2}. Similarly to H_2, we find that the C to CO transition happens at about 0.5 dex smaller $N_{\rm H}$ than MS05. Apart from the offset in $N_{\rm H}$ and the qualitative difference in $y({\rm C}^+)$, the results are very comparable.

3.1.2 *Model 2 (Fig. 2, top-right panel)*

At small $N_{\rm H}$ we find very similar results, except that $y(H_2)$ is smaller than MS05. The reason for this close agreement is probably that the gas is partially ionized and $T \sim 10^4$ K, and this convergence of electron fraction and temperature means that most quantities are comparable. At large $N_{\rm H}$ we see the same trends as for model 1, namely that the H to H_2 transition happens at smaller $N_{\rm H}$ in our calculations, by about 0.3 dex, and the same for the C to CO transition.

Model 2 has a weak discontinuity in T and $y(H_2)$ at $N_{\rm H} \approx 10^{23.5}$ cm^{-2}, which was not found by MS05. This is one of the more striking features of Fig. 2, and also appears in model 4 at $N_{\rm H} \approx 10^{21.2}$ cm^{-2}. Such discontinuities were also obtained by Yan (1997) for gas with sub-solar metallicity, and arise from a chemo-thermal instability that is associated with a region in $n - T$ space where H_2 is the dominant coolant (see also CLOUDY results in Section 3.2). These discontinuities are superficially reminiscent of an ionization front, where the thermal and ionization properties of a medium change very rapidly. In that case, however, the cross-section for absorption of ionizing photons is so large that there is very strong deposition of energy in a thin layer separating neutral from ionized gas. In contrast, the X-ray heating rate as a function of column density is unaffected by the chemo-thermal instability and remains a smooth function of $N_{\rm H}$.

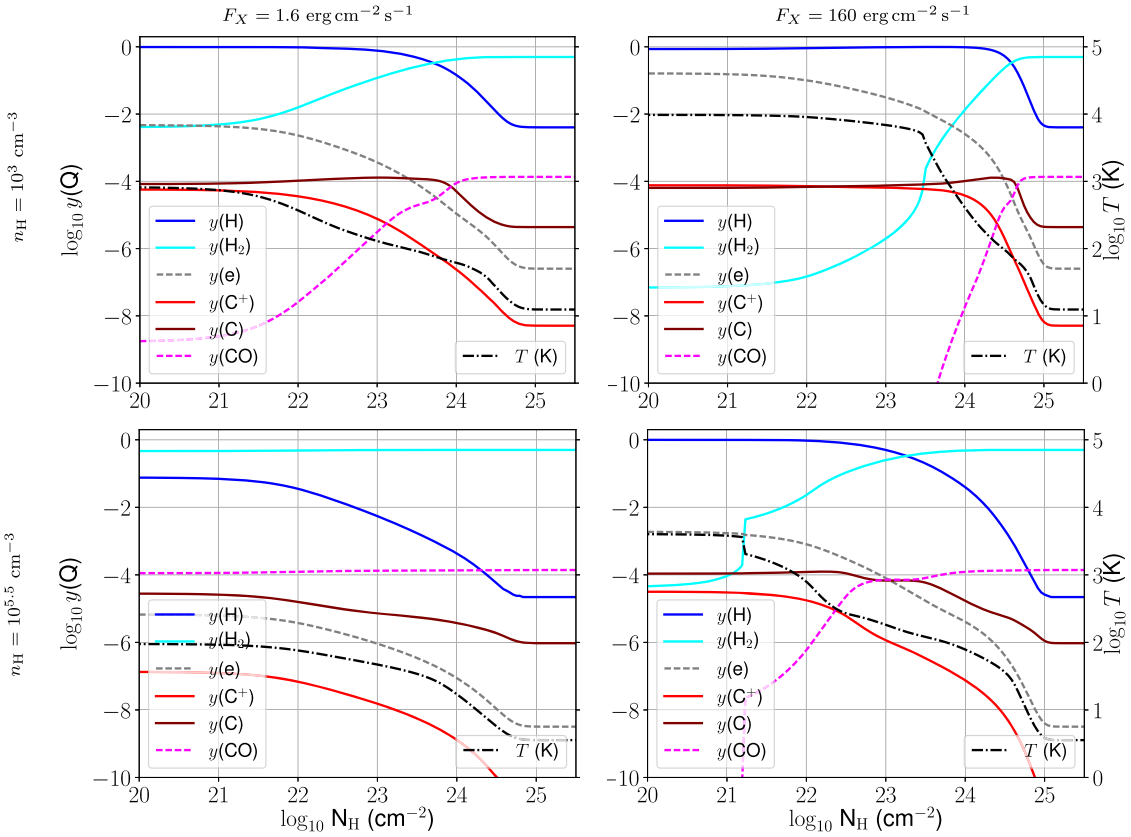

Figure 2. Results obtained for MS05 models 1 (upper left), 2 (upper right), 3 (lower left) and 4 (lower right; see Table 4 for the run parameters). The H, H_2, electron, C^+, C, and CO abundances, and gas temperature, T, are plotted as a function of column density, N_H, both on log scales. The left y-axis refers to abundances, and the right y-axis to temperature. The results can be compared with figs 3 and 4 of MS05.

3.1.3 Model 3 (Fig. 2, bottom-left panel)

This shows the largest discrepancies between our results and MS05. We find that the gas is mostly molecular at all column densities, and at small N_H we find that $y(H) \approx 0.08$ and $y(C) \approx 3 \times 10^{-5}$, whereas MS05 found that H and H_2 should have comparable abundances and that C should be more abundant than CO. They also found a larger electron fraction but comparable temperature. The difference seems to arise from the treatment of C^+: MS05 find $y(C^+) > 10^{-5}$ up to $N_H \approx 10^{24.5}$ cm^{-2}, whereas we have $y(C^+) \approx 10^{-7}$ at small N_H and decreasing as N_H increases. Consequently MS05 have a significantly larger electron fraction than we do, and this affects the chemical balance.

3.1.4 Model 4 (Fig. 2, bottom-right panel)

The asymptotic temperatures at low and high N_H are similar to MS05, and the run of T with N_H is also similar, although not identical. As mentioned above, there is a temperature discontinuity at $N_H \approx 10^{21.2}$ cm^{-2}, associated with a chemo-thermal instability. This was not found by MS05, and it is the most striking difference between our results and theirs. We again find that the atomic-to-molecular transition occurs at smaller N_H than MS05 by about 0.5 dex, and the temperature and electron fraction also decrease more rapidly with N_H. For example at $N_H = 10^{23}$ cm^{-2}, MS05 find $T \approx 10^3$ K and $y(e^-) \approx 10^{-3}$, whereas we find $T = 180$ K and $y(e^-) = 7 \times 10^{-5}$.

The broad agreement between our results and those of MS05 is encouraging, but there are systematic differences in the column density of the atomic-to-molecular transition, the abundance of $y(C^+)$ and the occurence of temperature discontinuities. This prompted a direct comparison with an XDR code that uses a much larger network, discussed in the next sub-section. We also present a study of the effects of the new reactions added to the NL99 network following Gong et al. (2017) in Appendix A. Regarding $y(C^+)$, the appendices show that the addition of new reactions following Gong et al. (2017) is driving the discrepancy, particularly the grain recombination reactions, without which we obtain similar C^+ abundances to MS05.

3.2 COMPARISON WITH CLOUDY

We also ran the same test problems with CLOUDY (Ferland et al. 2013), which has a more detailed treatment of X-ray absorption and ionization processes than our module and also a much larger chemical network. The calculations were performed with version 17.00 of CLOUDY as described by Ferland et al. (2013,2017). Note that even for the species that we have in common with the CLOUDY network, the reaction and cooling rates used may not be the same.

We use the standard CLOUDY mix of silicate and graphitic dust grains with a ratio of total to selective extinction of $R_V = 3.1$, which is typical for the ISM in the Milky Way in terms of abundance and size distribution (Mathis, Rumpl & Nordsieck 1977). Polycyclic aromatic hydrocarbons (PAHs) are not included. As in previous

Table 6. List of heavy elements included in the CLOUDY models (first column) sorted by their respective ionization potential (last column). The relative abundances with respect to hydrogen are given in the middle column.

Element	Abundance	Ionization potential
Sodium	3.16×10^{-7}	5.14 eV
Magnesium	1.26×10^{-5}	7.65 eV
Iron	6.31×10^{-7}	7.9 eV
Silicon	3.16×10^{-6}	8.15 eV
Sulphur	3.24×10^{-5}	10.36 eV
Carbon	1.40×10^{-4}	11.26 eV
Oxygen	3.40×10^{-4}	13.62 eV
Nitrogen	7.94×10^{-5}	14.53 eV
Helium	1.00×10^{-1}	24.59 eV

work (Walch et al. 2015) we set the overall dust-to-gas mass ratio to 0.01. We started from the full ISM model for the gas phase abundances and reduced the included heavy elements to the most important ones, i.e. the ones we find to be necessary in order to reproduce our results reasonably well (see Table 6, left column). All other elements were switched off but were thoroughly checked to only result in minor changes when included with their standard ISM gas phase abundances from CLOUDY. We find that magnesium and iron are most important for setting the electron abundance. The abundances of the elements that we do include are shown in Table 6, middle column.

In CLOUDY the ISRF is modelled as a blackbody with temperature 30 000 K in the energy range of 0.44–0.99 Rydberg as suggested by the CLOUDY documentation. The total intensity of the ISRF is scaled to the same value as used in Section 3.1, i.e. corresponding to a $G_0 = 10^{-6}$. All other initial conditions are also the same as in Section 3.1.

The results are plotted in Fig. 3, in a similar manner to Fig. 2. CLOUDY also obtains the chemo-thermal instability for models 2 and 4. It occurs at the same $N_{\rm H}$ as what we find for model 2, but the jump in T and $y(H_2)$ is larger. For model 4 CLOUDY finds a weaker discontinuity that occurs at larger $N_{\rm H}$ than in our calculations.

For hydrogen, the atomic-to-molecular transition happens at similar $N_{\rm H}$ for CLOUDY and our code, and the H_2 abundance is comparable in both calculations for all models. The biggest difference is for model 2, where $y(H_2)$ increases more rapidly with $N_{\rm H}$ in the CLOUDY calculation and the H→H_2 transition occurs at smaller $N_{\rm H}$ (by ∼0.5 dex). This is the opposite of what we found comparing with MS05, where they found the transition at larger $N_{\rm H}$ than our results by ∼0.5 dex.

The gas temperature from our calculations agrees well with CLOUDY for models 1 and 2, but for models 3 and 4 CLOUDY finds larger temperature than our module in the range $21.5 \lesssim \log N_{\rm H}/{\rm cm}^{-3} \lesssim 24.5$. The electron fraction is also larger in this range. The temperature discrepancy is up to 0.5 dex for model 4.

The results for carbon-bearing species are plotted in Fig. 4. CLOUDY can include freeze-out of molecules on to grains, which is not in our network, so we switched this off for the comparison. The CO abundance agrees well for all calculations in Figs 3 and 4. In the CLOUDY results, the dip in CO abundance just below $N_{\rm H} \approx 10^{24}\,{\rm cm}^{-2}$ in model 1 (slightly larger $N_{\rm H}$ in model 2) is because of CS formation at this depth, which is not in our network. In models 1 and 2 the CLOUDY abundance of CO increases more rapidly with $N_{\rm H}$ than what we find, but the opposite is true in model 4. The abundances of atomic C and C^+ generally agree well between the two networks, but the limiting y(C) at large $N_{\rm H}$ is much lower in the CLOUDY results for models 3 and 4. We find generally smooth and monotonic curves for C^+, C, and CO, with at most a single maximum for y(C), whereas CLOUDY has more pronounced maxima and other features. This is probably due to interaction with other carbon-bearing species that are not included in our network. Notably, the agreement with CLOUDY is better than with MS05, suggesting that updated reaction and cooling rates over the past 13 yr have a bigger impact on our results than the size of the chemical network.

In summary, our results for the H → H_2 and $C^+ \rightarrow C \rightarrow CO$ transitions agree well with results obtained from CLOUDY, with small differences in the exact value of $N_{\rm H}$ for each transition. The temperature and electron fractions as a function of $N_{\rm H}$ also agree well with some caveats, notably the discrepancy in model 4. Less abundant species (CH_x, OH_x, HCO^+) are poorly predicted by our simple reaction network, probably because these are primarily included in the network in order to obtain the correct relative abundances of C^+, C, and CO. These trace species are not the focus of this work.

3.3 TESTS OF ENERGY RESOLUTION

We ran a large grid of 1D models with varying ISM density, X-ray flux, and X-ray spectrum. Density varies from $n_{\rm H} = [0.1-10^6]\,{\rm cm}^{-3}$, flux from $F_X = [10^{-5}-10^5]\,{\rm erg\,cm}^{-2}\,{\rm s}^{-1}$, and blackbody spectra with radiation temperature $E_{\rm rad} = [0.1-10]$ keV. This was used to validate the code over a large range of different conditions, find any regions of parameter space where the ODE solver fails to converge, and test how many energy bins are required for different ISM conditions. A sample of results are shown in Fig. 5, for a fixed gas density ($n_{\rm H} = 10^4\,{\rm cm}^{-3}$), two different X-ray fluxes and two different radiation temperatures, $E_{\rm rad}$ (for a blackbody spectrum). All of these calculations have a UV radiation field of $G_0 = 1$, which is why the CO abundance is low at low column density.

The models of MS05 (Section 3.1) had $G_0 = 10^{-6}$, and so the gas could be fully molecular at low column density for model 3. Apart from this, the low-flux calculations in Fig. 5 have many similarities to model 3. The high-flux calculations are most similar to model 4, but the flux is significantly higher. In these extreme conditions the energy resolution plays a key role because the cross-section of the softest (hardest) energy bin increases (decreases) as the energy bin gets narrower.

For all plotted calculations, 2 energy bins (0.1–1 and 1–10 keV, dotted lines) are rather crude approximation and some atomic-to-molecular transitions happen at quite different column densities for $F_X = 10^5\,{\rm erg\,cm}^{-2}\,{\rm s}^{-1}$. For the low-flux calculations, 6 energy bins (dashed lines) are sufficient in all cases and seem adequate but not ideal for the high-flux calculations. The transitions between different phases (ionized-to-atomic, atomic-to-molecular) happen at column densities differing by up to 0.1 dex between 6 and 20 energy bins, whereas the difference can be up to 1 dex between 2 and 20 bins.

The tradeoff between number of energy bins and computational cost (memory and cpu cycles) means that we have to accept some level of error from using discrete energy bins. The worst case found on the grid of calculations was for $E_{\rm rad} = 10$ keV and $F_X = 10^5\,{\rm erg\,cm}^{-2}\,{\rm s}^{-1}$, i.e. gas irradiated very strongly by a hard X-ray field. In this case the location of the atomic-to-molecular transition differed by about 0.1 dex between 6 and 20 energy bins. This is because there is a lot of flux in the highest-energy bin for such a hard spectrum, and so its cross-section is a key to determining the column density at which X-ray heating becomes ineffective. For the calculations in the next sections we use a thermal spectrum with

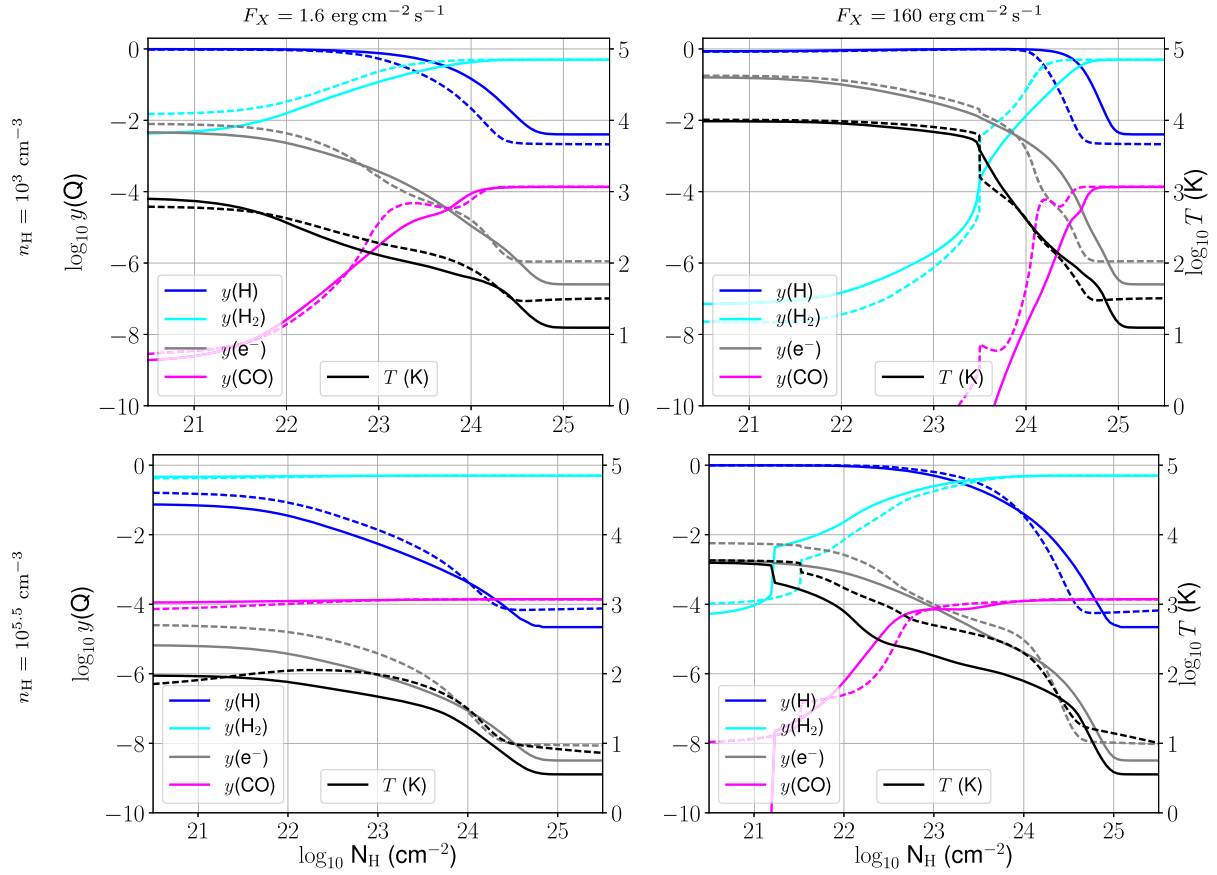

Figure 3. Abundances of H_2, CO, H, electrons, and gas temperature for models 1 (upper left), 2 (upper right), 3 (lower left), and 4 (lower right) calculated using CLOUDY (dashed lines) and compared with our calculations (solid lines). The results are plotted as a function of column density of hydrogen. The left-hand vertical axis shows the fractional abundance whereas the right-hand vertical axis shows the temperature scale.

$T = 1$ keV, and so this problem is not so severe because there is very little flux in the highest energy bins.

4 IRRADIATION OF A FRACTAL CLOUD

We added the new chemistry network to the FLASH code, as discussed in Section 2; this was implemented in a similar way to how the NL97 network (Nelson & Langer 1997; Glover & Clark 2012) has been used for the SILCC simulations (Walch et al. 2015). Multiple chemical species are implemented using the FLASH Multispecies framework, and radiative transfer uses TREERAY (Wünsch et al. 2018).

We follow Shadmehri & Elmegreen (2011) and Walch et al. (2012) to set-up a fractal density field with a given fractal index D_f and a lognormal density probability density function (PDF). The fractal density field is set-up in Fourier space using a power-law distribution of the amplitude squared, $A^2_{\rho(k)} \propto k^{-n}$ on all modes ranging from 1 to 128. The power spectral index n is related with D_f through $D_f = 4 - \frac{n}{2}$. Here we choose $D_f = 2.5$ and hence $n = 3.0$, typical for molecular clouds in the Milky Way (Stutzki et al. 1998). The simulation box is a cube of diameter 25.6 pc and we use a uniform grid with 256^3 grid cells, so the grid cell-size is 0.1 pc, sufficient to resolve the CO chemistry (Seifried et al. 2017). The total mass in the box is 10^5 M$_\odot$ and the maximum density located at the origin of the computational domain is $\rho_{\rm max} = 1.6 \times 10^{-20}$ g cm^{-3}.

Nine different simulations were run without hydrodynamics, labelled F0–F8, each with a different X-ray flux irradiating the outer boundary given in Table 7. Recall that this flux is equal to $\sum_{i=1}^{N_E} 4\pi J_{X,i}$ where $J_{X,i}$ is the mean intensity of the isotropic radiation field in energy bin i. The hydrodynamic boundary conditions are irrelevant for the calculation, and as noted above we use isolated boundaries for the TREERAY algorithm. We consider a thermal X-ray spectrum between 0.5 and 15 keV, with a temperature of 1 keV. Six new scalar field variables are added to account for the attenuation of the six logarithmically spaced X-ray energy bins, with energy limits and mean cross-sections in each bin given in Table 8. The unattenuated X-ray flux and energy density in each energy bin is also quoted for simulation F5 in Table 8; for other simulations these values can be scaled, e.g. F0 is scaled down by 10^5 and simulation F8 is scaled up by 10^3. This table shows that the energy range 0.5–15 keV covers almost all of the emission for the 1 keV blackbody that we consider; adding further energy bins above or below this range would add less than 1 per cent to the total X-ray energy density. Fig. 6 plots the UV and X-ray flux for each of the 9 simulations, as well as the continuous and discrete cross-section for X-ray absorption. For simulation F4 the discrete flux in each bin is also shown as the brown dashed line, converted to the appropriate units by multiplying the flux by the mid-point energy of the bin. The external UV radiation field is set to $G_0 = 1.7$ in units of the Habing field, corresponding to the Draine (1978)

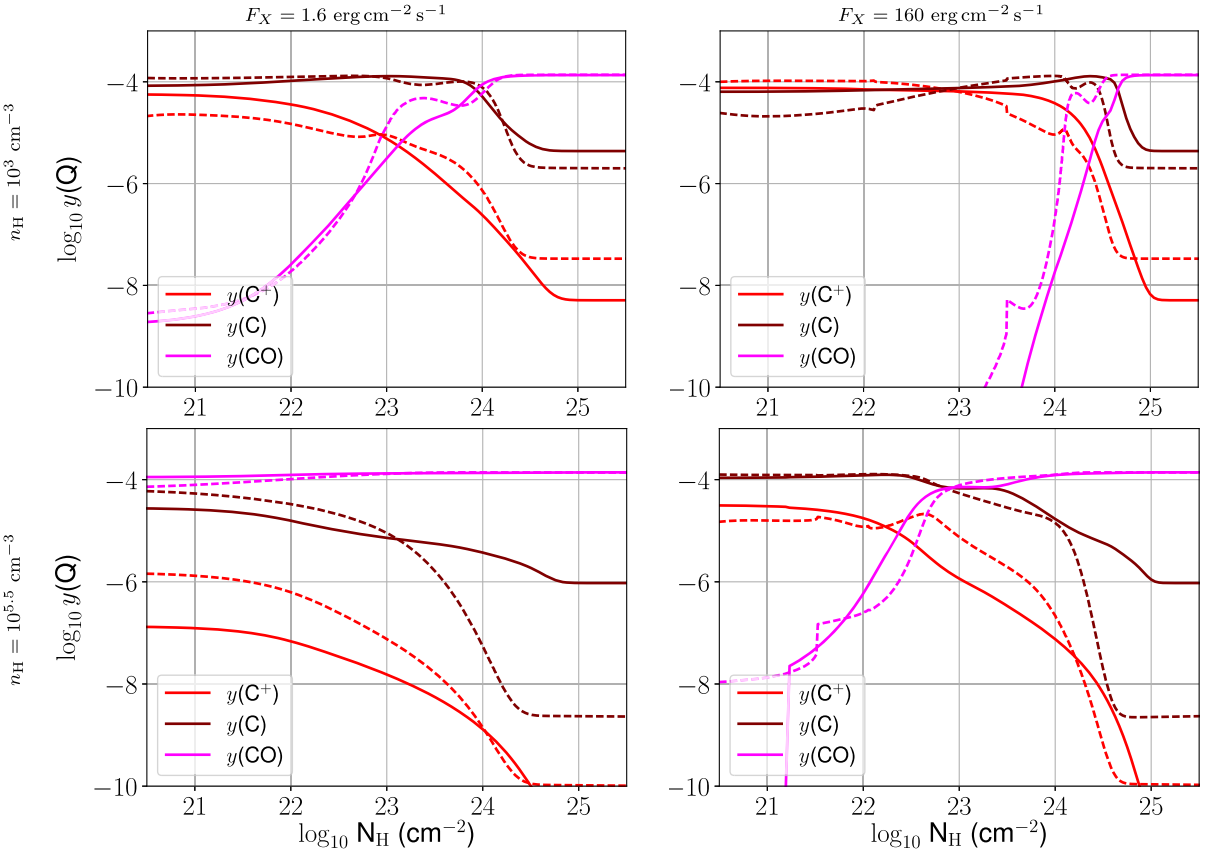

Figure 4. Same as Fig. 3 but for the main carbon-bearing species included by the network: abundances of C^+, C, CO for the 4 models. The dashed lines show the results of the CLOUDY calculation and the solid lines show our results.

field, and is not scaled with the X-ray field strength but rather kept constant.

For each simulation, we start with constant temperature 1423 K (sound speed of 3 km s^{-1}) and uniform number fractions of $y(H_2) = 10^{-5}$, $y(H^+) = 0.1$, and $y(CO) = 10^{-8}$. We assume the rest of the carbon is in the form of C^+, that helium is neutral, and that the metal, M, is in the form of M^+. The simulation is then run so that it evolves chemically and thermally towards equilibrium for 4 Myr. The dense regions have reached equilibrium by this time, but the lowest density gas is still evolving slowly.

4.1 Physical state of the gas

Fig. 7 plots the location of the grid cells in the density–temperature plane for simulations F0–F8; effectively an unnormalized, volume-weighted, probability distribution function (PDF) in density and temperature. Brighter colours indicate regions with more cells. Similarly, Fig. 8 plots the same in the extinction–temperature plane. It is important to note that different cells in our 3D simulations experience different UV extinction factors and so the equilibrium temperature depends on both density and location. Once chemical and thermal equilibrium has been reached, the cells all sit on a surface in the space of density, temperature, and UV extinction, and Figs 7 and 8 are projections of this surface on to two different planes. The scatter in these plots arises from this projection and not from the gas being out of equilibrium. For larger X-ray flux the UV field has decreasing importance and so the effect of extinction on equilibrium temperature starts to drop out.

The extinction, A_V, is calculated using equation (8), but for the UV ISRF rather than X-ray radiation field. This is

$$\langle A_V \rangle = -\frac{1}{2.5} \log \frac{1}{N_{pix}} \sum_{i=1}^{N_{pix}} \exp\left(-2.5 A_V^i\right), \quad (17)$$

where A_V^i is the visual extinction along ray i, and N_{pix} is the number of rays used to sample all directions in 3D space (here $N_{pix} = 48$, see Section 2.1). Due to the non-linear nature of this equation, the resulting average $\langle A_V \rangle$ is dependent on the radiation energy at which the average is taken, i.e. dependent on the numerical multiplier that here is 2.5, appropriate for the UV ISRF. Using the attenuation from one of the X-ray energy bins, or indeed the visual attenuation (a numerical multiplier of unity) gives a different mean value. This shows the importance of 3D simulations: for a 1D calculation the extinction is a single number, but for 3D simulations the weighting of different rays is wavelength dependent, and so the mean UV or X-ray extinction is not necessarily consistent with what one expects given the mean optical extinction.

There is very little difference between F0 and F1 in Fig. 7, because the X-ray field is weak and cannot affect the chemistry or thermal state of the gas to any significant extent (a run with zero X-ray flux is almost identical to F0 in these plots). Almost all of the gas is in the temperature range 7–100 K, and there is a relatively weak correlation between temperature and density (multiple temperatures

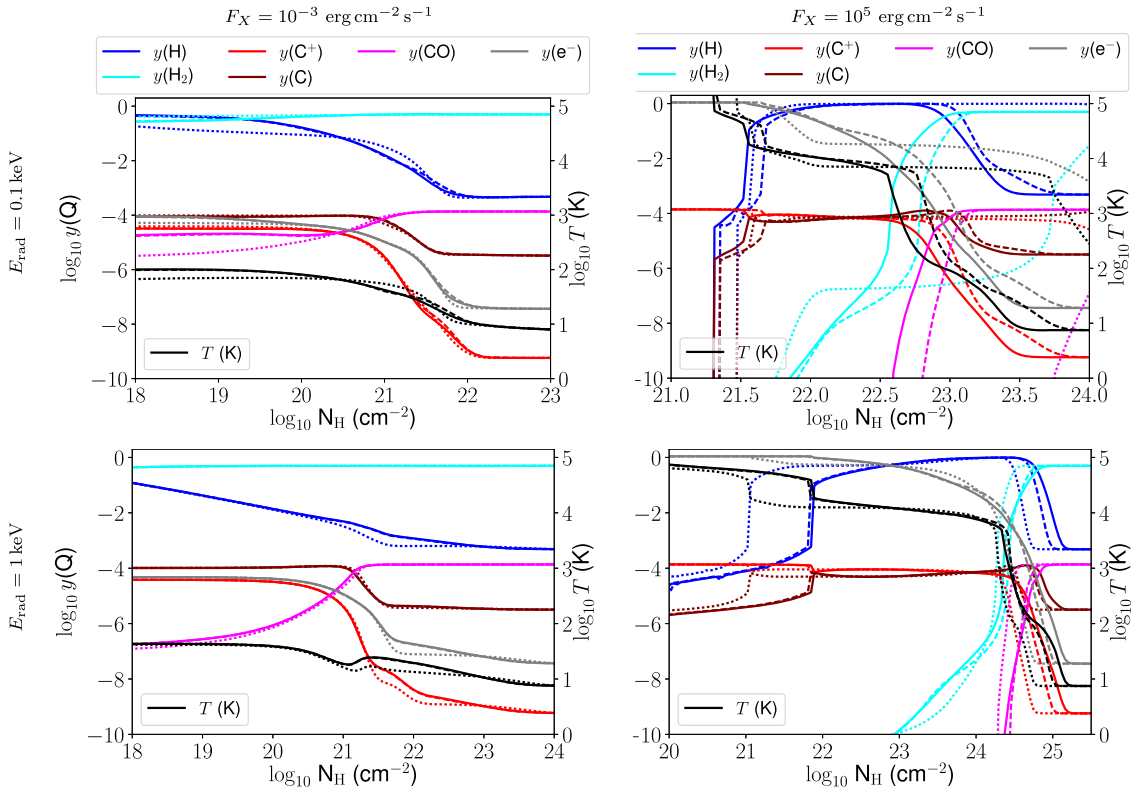

Figure 5. Abundances of H^+, H, H_2, C^+, C, CO, electrons, and gas temperature for a set of 1D calculations using different X-ray fluxes and radiation temperature. Dotted lines are results using two energy bins in 0.1–10 keV, dashed lines using 6, and solid lines using 20. The results are plotted as a function of column density of hydrogen nuclei. In each case the gas has number density $n_{\rm H} = 10^4$ cm^{-3}. The left-hand vertical axis shows the fractional abundance whereas the right-hand vertical axis shows the temperature scale.

Table 7. X-ray fluxes and energy densities considered in each of the simulations in Section 4.

Simulation	Flux (erg cm^{-2} s^{-1})	$E_{\rm rad}$ (erg cm^{-3})
F0	10^{-5}	3.3×10^{-16}
F1	10^{-4}	3.3×10^{-15}
F2	10^{-3}	3.3×10^{-14}
F3	10^{-2}	3.3×10^{-13}
F4	10^{-1}	3.3×10^{-12}
F5	10^{0}	3.3×10^{-11}
F6	10^{1}	3.3×10^{-10}
F7	10^{2}	3.3×10^{-9}
F8	10^{3}	3.3×10^{-8}

are found for gas at a given density). In contrast, there is a strong correlation between temperature and extinction, $A_{\rm V}$, for these simulations (Fig. 8), with temperature decreasing strongly with increasing extinction and most cells following a single curve in the plane.

Simulation F2 is a transitional case, where the X-ray field has a noticeable effect on the gas temperature but where the temperature is still strongly correlated with $A_{\rm V}$. The minimum temperature at large column density (where X-ray heating is effective) is increased to >10 K with respect to F0 and F1, but the temperature at low column density (where UV heating is effective) is similar to F0 and F1. There is similar energy in both the UV and X-ray fields ($F_X \approx 10^{-3}$ erg cm^{-2} s^{-1}) and so both have similar levels of influence. The majority of the UV energy is deposited at $A_{\rm V} < 1$ near the cloud surface, whereas the X-ray energy penetrates beyond $A_{\rm V} = 10$ and so it acts on the whole cloud.

The thermodynamics of the remaining simulations are all dominated by the X-ray radiation field. The mean temperatures of F3 and F5 are 100 and 8 000 K, respectively, with very little dependence on extinction (Fig. 8). Simulation F4 has significant quantities of gas at all temperatures from 100 to 8 000 K, regardless of $A_{\rm V}$. This is because the cloud is optically thin to X-rays in the higher energy bins (>1 keV), and so the heating rate of a cell depends on the cell density to a much greater extent than the cell's $A_{\rm V}$. Fig. 7 reflects this, showing very tight correlations between gas density and temperature for F4–F8. For F5 ($4\pi J_X = 1$ erg cm^{-2} s^{-1}) there are two regimes, where gas with $\rho \lesssim 10^{-21}$ g cm^{-3} is at $T \sim 10^4$ K, whereas higher density gas has progressively lower temperature. For F4 the dividing line is $\rho \sim 10^{-22}$ g cm^{-3}, and for F3 it is about $\rho \sim 10^{-23}$ g cm^{-3}. This reflects the fact that the cooling rate increases dramatically at $T \sim 10^4$ K, with Lyman α and forbidden-line cooling becoming very strong. The cooling rate scales with $n_{\rm H}^2$ whereas X-ray heating scales with $n_{\rm H}$, and so the density at which the Lyman α and forbidden-line cooling equals the heating rate should scale with $4\pi J_X$. At higher densities the temperature decreases with increasing density.

Simulations F6–F8 have sufficiently strong X-ray fields that the heating rate is stronger than the Lyman α cooling rate, and so much of the gas becomes highly ionized with $T > 10^4$ K. With such high temperatures the molecules in these simulations are destroyed, and the chemistry network that we use is no longer well-suited to the physical conditions because we do not include higher ionization

Table 8. Energy limits, mean absorption cross-section $\langle\sigma\rangle$, X-ray radiation flux $4\pi J_{X,\,i}$, and X-ray energy density $E_{\rm rad}$ for the six energy bins used in the 3D FLASH simulations. The radiation flux and energy density are quoted for simulation F5, and are scaled up or down by powers of 10 for the other simulations.

Bin	$E_{{\rm min},\,i}$ (keV)	$E_{{\rm max},\,i}$ (keV)	$\langle\sigma_i\rangle$ (cm^{-2})	$4\pi J_{X,\,i}$ (er g cm^{-2} s^{-1})	$E_{{\rm rad},\,i}$ (er g cm^{-3})
0	0.500	0.881	5.84×10^{-22}	1.97×10^{-2}	6.57×10^{-13}
1	0.881	1.554	1.43×10^{-22}	7.85×10^{-2}	2.62×10^{-12}
2	1.554	2.739	3.49×10^{-23}	2.34×10^{-1}	7.81×10^{-12}
3	2.739	4.827	8.54×10^{-24}	3.98×10^{-1}	1.33×10^{-11}
4	4.827	8.510	2.09×10^{-24}	2.42×10^{-1}	8.09×10^{-12}
5	8.510	15.000	5.10×10^{-25}	2.76×10^{-2}	9.20×10^{-13}

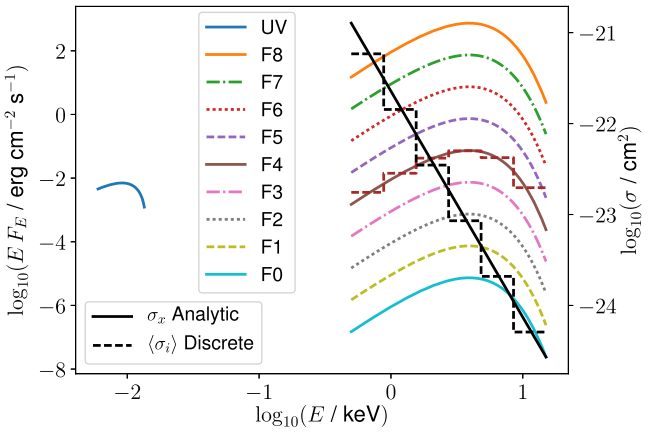

Figure 6. UV flux (blue) and X-ray flux from Table 7 for the 9 simulations in Section 4 (left y-axis) and X-ray absorption cross-section (right y-axis). The continuous flux is plotted in all cases, and the discrete flux for simulation F4 using the dashed brown line. E is energy in keV and F_E is energy flux in units erg cm^{-2} s^{-1} keV^{-1}. For the cross-section, the continuous black line plots equation (1) from Panoglou et al. (2012), and the dashed black line the discrete cross-section used for each of the six energy bins.

stages of important coolants such as C, N, O, Fe, etc. The empty region in the plots for F6–F8 at $4.6 \lesssim \log T \lesssim 4.8$ is an artefact of this limitation of the network. For $T \gg 10^4$ K we assume cooling appropriate for collisional ionization equilibrium (interpolated from a table; see Walch et al. 2015), which is not satisfied for X-ray irradiated gas, and so the cooling rate has an incorrect temperature dependence. For sufficiently large X-ray heating rates this leads to runaway heating, and so we set the net heating rate to zero for $T > 10^5$ K in these simulations, because we are not interested in the coronal gas that X-ray heating can produce. Simulation F6 also has a gap around $T \sim 10^{3.5}$ K, which is a manifestation of the chemo-thermal instability seen in MS05 models 2 and 4. The gap is also seen in the T-$y(\mathrm{H_2})$ plane.

4.2 Chemical state of the gas

Fig. 9 plots the CO abundance, y(CO), in each cell as a function of $A_{\rm V}$ for simulations F0–F5 (F6–F8 have very little CO). Simulations F0 and F1 are showing what is typically found in PDR simulations, where the molecular fraction increases with column density, and increases dramatically once the column density is sufficient for self-shielding (see e.g. Tielens & Hollenbach 1985; Röllig et al. 2007).

In the remaining simulations (F2–F5) we see the increasingly strong effect of X-ray ionization and heating. As well as a general decrease in CO abundance at all column densities, the highly molecular gas at large column density progressively decreases with increasing flux, and disappears almost completely for F5. The CO abundance as a function of the H_2 abundance is plotted in Fig. 10, again only for simulations F0–F5. As the X-ray flux increases, the correlation between y(CO) and $y(\mathrm{H_2})$ gets stronger, and the overall CO abundance decreases. The correlation of CO abundance with H_2 abundance is stronger than that with $A_{\rm V}$, and this is again because the hard X-rays can penetrate to large $A_{\rm V}$. They are not strongly attenuated by the cloud that we simulate here, and so the thermal and chemical properties of a cell are set much more by the gas density than by the extinction. The CO abundance increases with the square of the H_2 abundance.

4.3 Column density maps of CO and H_2

In Fig. 11, we show the column density of H_2 and CO, and the column-density ratio of the two, for simulations F0–F5. Runs F1 and F2 are not shown because they are similar to F0, and F6–F8 are also not shown because they have very little CO (F7 has no cells with $y(\mathrm{CO}) > 3 \times 10^{-8}$, F6 has only a handful with $y(\mathrm{CO}) > 10^{-6}$).

Visual inspection of these figures shows that CO and H_2 start to be depleted for $4\pi J_X \gtrsim 10^{-1}$ erg cm^{-2} s^{-1} (F4) and are mostly destroyed for $4\pi J_X \gtrsim 1$ erg cm^{-2} s^{-1} (F5). CO also is destroyed more completely than H_2 for large X-ray fluxes: the mass ratio of CO to H_2 in the simulation box decreases from about 10^{-3} for F0–F4 to 3.7×10^{-4} for F5, 1.1×10^{-4} for F6, 1.4×10^{-5} for F7, and F8 has no CO. In simulation F3 the densest regions still have large CO column densities and, counter-intuitively, the lowest column density regions at the edges of the simulation box have more CO in F3 than in F0. The effect of X-rays is to raise the gas and dust temperatures (speeding up most reactions) and to increase the abundance of electrons and ions that are required for the formation of CO.

Fig. 12 shows the total mass fractions of various chemical species in the simulation domain for simulations F0–F8, again at $t = 4$ Myr, with the X-ray flux on the x-axis. For low fluxes, the CO mass fraction actually increases slightly with increasing X-ray flux (already seen in Fig. 11 and discussed above), along with CH_x, OH_x, and HCO^+. All molecular species are destroyed with increasing flux following similar trends and beginning at the same flux value: $4\pi J_X > 10^{-2}$ erg cm^{-2} s^{-1} (F3). H_2 is more resistant for large X-ray fluxes than any other molecule, surviving at trace levels up to the highest X-ray fluxes, whereas CO and the other molecular species are completely destroyed for $4\pi J_X > 10^2$ erg cm^{-2} s^{-1} (F7). The reason for this can be seen in the temperature panel, where the mean temperature approaches 10^4 K for $4\pi J_X > 1$ erg cm^{-2} s^{-1}, and the minimum temperature jumps from $\sim 10^2$ K to nearly 10^4 K between $4\pi J_X = 10$ and 10^3 erg cm^{-2} s^{-1}. Most of the destroyed CO goes into increasing the C^+ abundance, but this has a small

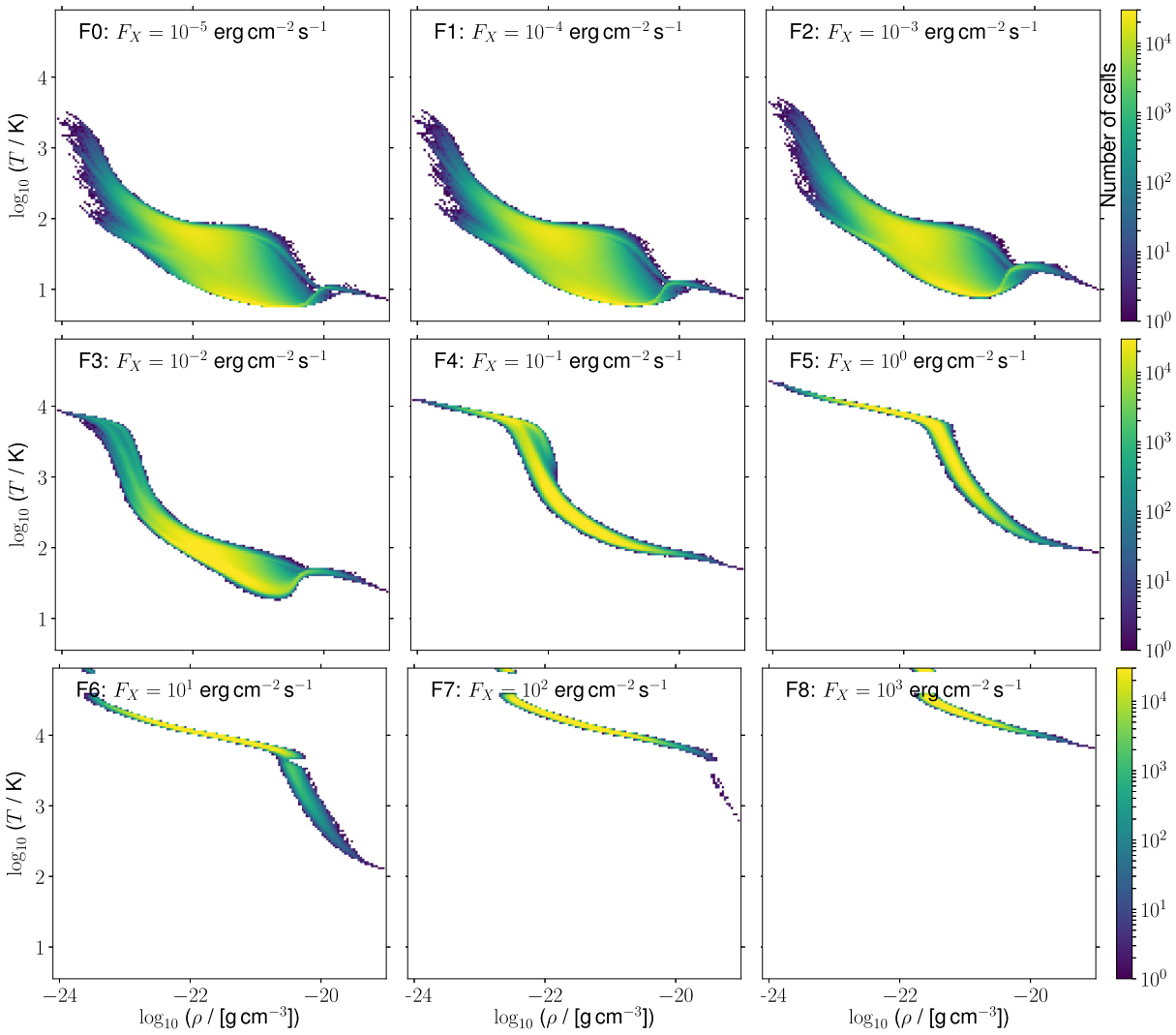

Figure 7. Volume-weighted (unnormalized) temperature-density PDF of the fractal cloud, where the logarithmic colour scale indicates the number of grid cells at a given point in the parameter space. Each panel has a different X-ray irradiating flux, with increasing X-ray flux from left to right and top to bottom (F0–F8, see Table 7). There are 256^3 cells in total, each with volume 10^{-3} pc^3. For weak X-ray irradiation, cells with different extinction can have different equilibrium temperatures for a given density, whereas with strong X-ray irradiation the temperature is almost entirely determined by density alone.

effect on the total electron abundance because most electrons are produced from H^+ and He^+ for $4\pi J_X > 10^{-2}$ erg cm^{-2} s^{-1}. Neutral carbon also decreases in abundance with increasing $4\pi J_X$, albeit with a much weaker dependence on $4\pi J_X$ than CO.

5 FLARING X-RAY SOURCES

5.1 Effect of increasing the X-ray irradiation

Here we study the effects of a strong X-ray radiation field that is switched on for a given length of time and then switched off (i.e. a flare) to see how the chemistry of a molecular cloud responds. We take as initial conditions the cloud in simulation F2, where the chemistry and thermodynamics have been allowed to relax towards equilibrium for 4 Myr. We then increase the X-ray flux instantaneously by a factor of 10^5, from $4\pi J_X = 10^{-3}$–10^2 erg cm^{-2} s^{-1}. This large flux is similar to models 2 and 4 in MS05, who chose this value because it is typical of the cloud irradiation near AGN (it is also what is used in our simulation F7). Because the speed of light is considered to be infinite, this affects all parts of the simulation instantaneously, heating, ionizing atoms, and dissociating molecules. Note that we find strong chemical and thermal effects on time-scales shorter than the light-crossing-time of the simulation domain (i.e. 100 yr). The actual thermal and chemical effects we see on the cloud are robust, but the time-lag would be slightly different if we had a greater level of realism in modelling the radiative transfer.

The evolution of the mass fractions of ions and molecules as a function of time, as well as the mean temperature, are plotted in Fig. 13. The mass fractions of H^+ and He^+ increase rapidly because of the dramatically increased ionization rate until they saturate at their equilibrium values after about 3×10^3 yr. Carbon goes from being partially ionized to almost fully ionized throughout the whole simulation after about 10 yr, and the equilibrium mass fraction of C^+ at $t > 10^3$ yr is slightly larger than, but comparable to, that of neutral carbon. The metal (M) is almost fully ionized in the initial conditions, and so its ionization state doesn't change much.

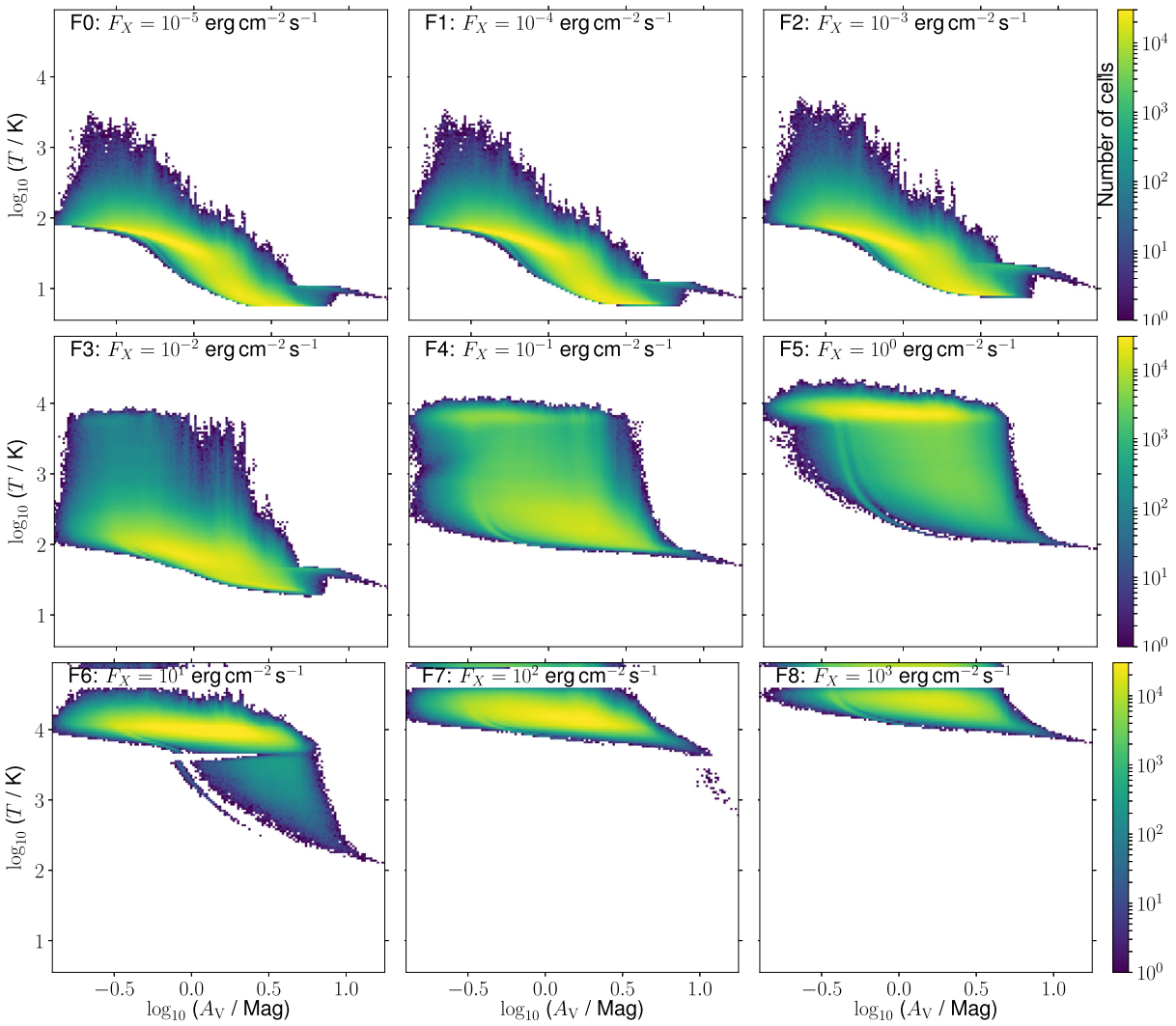

Figure 8. Volume-weighted (unnormalized) PDF in the plane of local extinction, A_V, and temperature, T, for the fractal cloud, where the logarithmic colour scale indicates the number of grid cells at a given point. Each panel has a different X-ray irradiating flux, with increasing X-ray flux from left to right and top to bottom (F0–F8). The A_V value is calculated from the angle-averaged attenuation factor of the cell (equation 17).

The results for the molecules are more interesting and subtle. The middle panel of Fig. 13 shows that CO is very rapidly destroyed between 1 and 20 yr after the X-ray flare switches on, and after about 20 yr its rate of destruction decreases noticeably. HCO^+ follows the same trend, whereas CH_x and OH_x are destroyed more gradually. H_2 is almost unaffected for 100 yr, and is significantly destroyed only after 10^3 yr. This means that an X-ray flare can destroy almost all of the CO in a molecular cloud, while leaving the H_2 unaffected if it is shorter than $\sim 10^3$ yr.

This surprising result can be explained by looking at the temperature dependence of the various creation and destruction reactions for CO. The mass-weighted mean temperature shows a rapid rise from $\approx$30 K initially to $\approx$100 K after 1 yr to $\approx$1000 K after 10 yr. This increase in temperature affects the dominant creation and destruction reaction rates for CO in a different way to H_2, with the result that the CO abundance is much more sensitive to cloud heating than the H_2 abundance for $T \lesssim 1000$ K.

At early times the main creation reaction is through $HCO^+ + e^-$ (Table A1, #38), and destruction is through H_3^+ (Table A1, #24). This pair of reactions is circular, however, and largely just convert CO to HCO^+ and back again, rather than reducing the overall quantity of CO. The H_3^+ destruction rate is constant, whereas the destruction through locally generated FUV by fast electrons (Table A2, #74) increases with temperature, so as the gas heats up, the FUV destruction becomes dominant after 1 yr. The creation rate (#38) decreases as T increases, so there is a phase of runaway CO destruction as long as these two (#38 and #74) are the dominant rates and T is increasing with time. During this phase the HCO^+ abundance decreases because it is being converted to CO through reaction #38 whereas the reverse reaction (#24) is no longer effective. The abundances of CH_x and OH_x are not so dramatically affected because the FUV destruction reactions (#75 and #76 in Table A2) are independent of temperature, unlike the CO destruction rate.

After about 10 yr, the HCO^+ creation channel for CO (#38) becomes too small, and the main creation rates are the constant rate from $CH_x + O$ (#36) to $OH_x + C$ (#37). This slows down the CO destruction because after 10 yr T remains relatively constant, and so the FUV destruction rate (#74) scales with the decreasing CO abundance. Only after >100 yr does the CO $+ He^+$ destruction

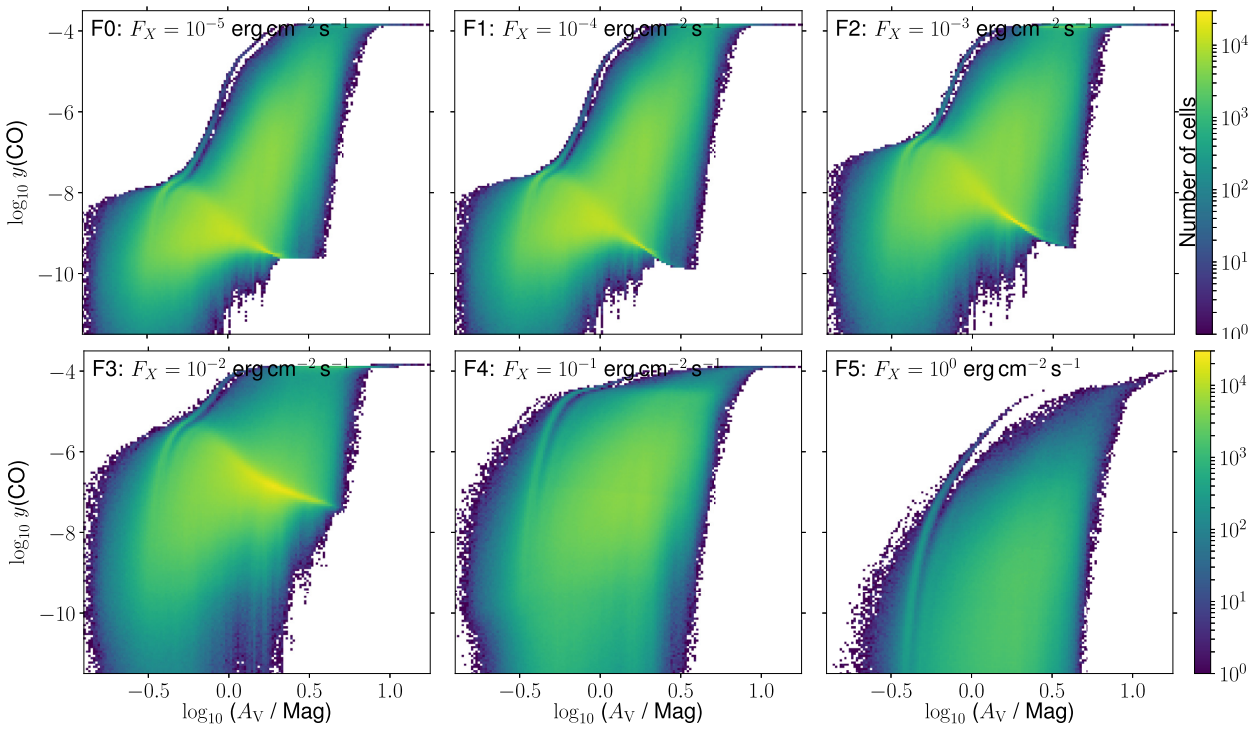

Figure 9. Volume-weighted (unnormalized) PDF in the plane of CO number fraction relative to H, y(CO), and local extinction A_V for the fractal cloud, where the logarithmic colour scale indicates the number of grid cells at a given point. Each panel has a different X-ray irradiating flux, with increasing X-ray flux from left to right and top to bottom (F0–F5). Simulations F6–F8 have so little CO that they are not shown. The A_V value of each cell is calculated from the angle-averaged attenuation factor of the cell (equation 17).

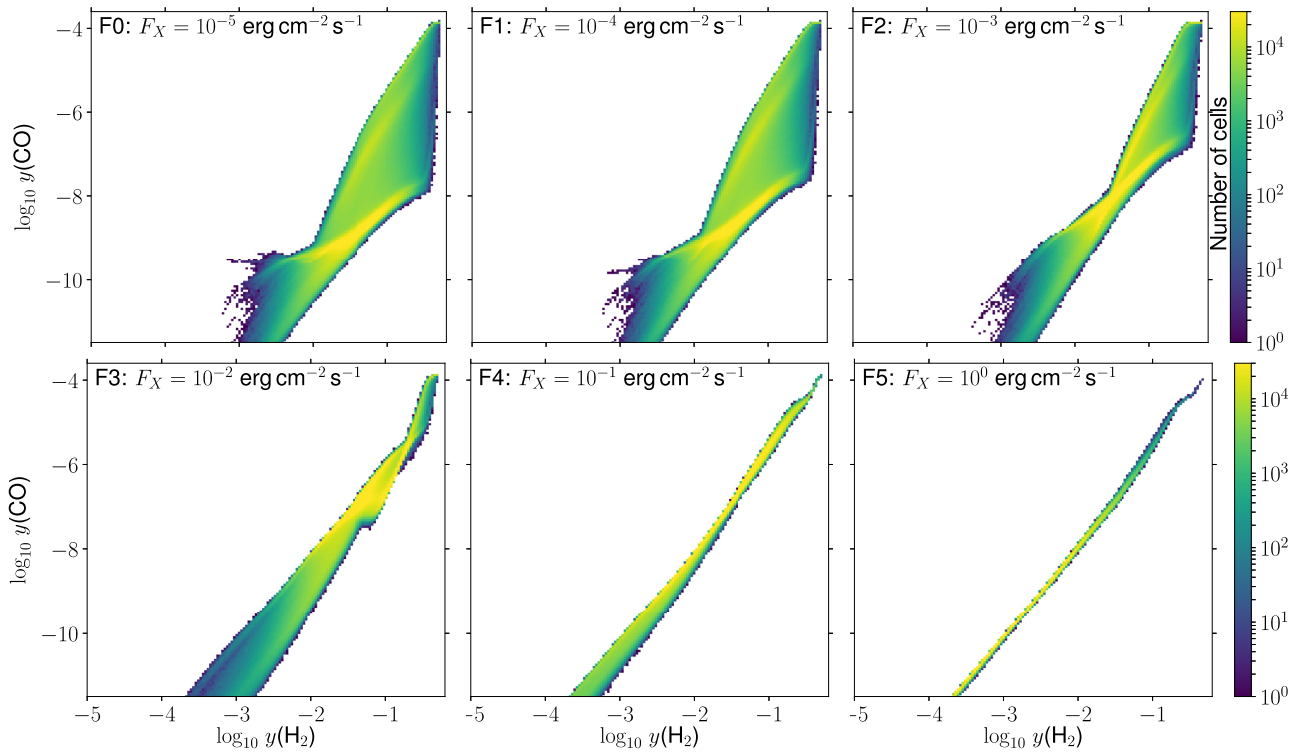

Figure 10. Volume-weighted (unnormalized) PDF in the plane of CO number fraction, y(CO), and H_2 number fraction, $y(H_2)$, for the fractal cloud, where the logarithmic colour scale indicates the number of grid cells at a given point. Each panel has a different X-ray irradiating flux, with increasing X-ray flux from left to right and top to bottom (F0–F5). Simulations F6–F8 had very little CO and so are not plotted here.

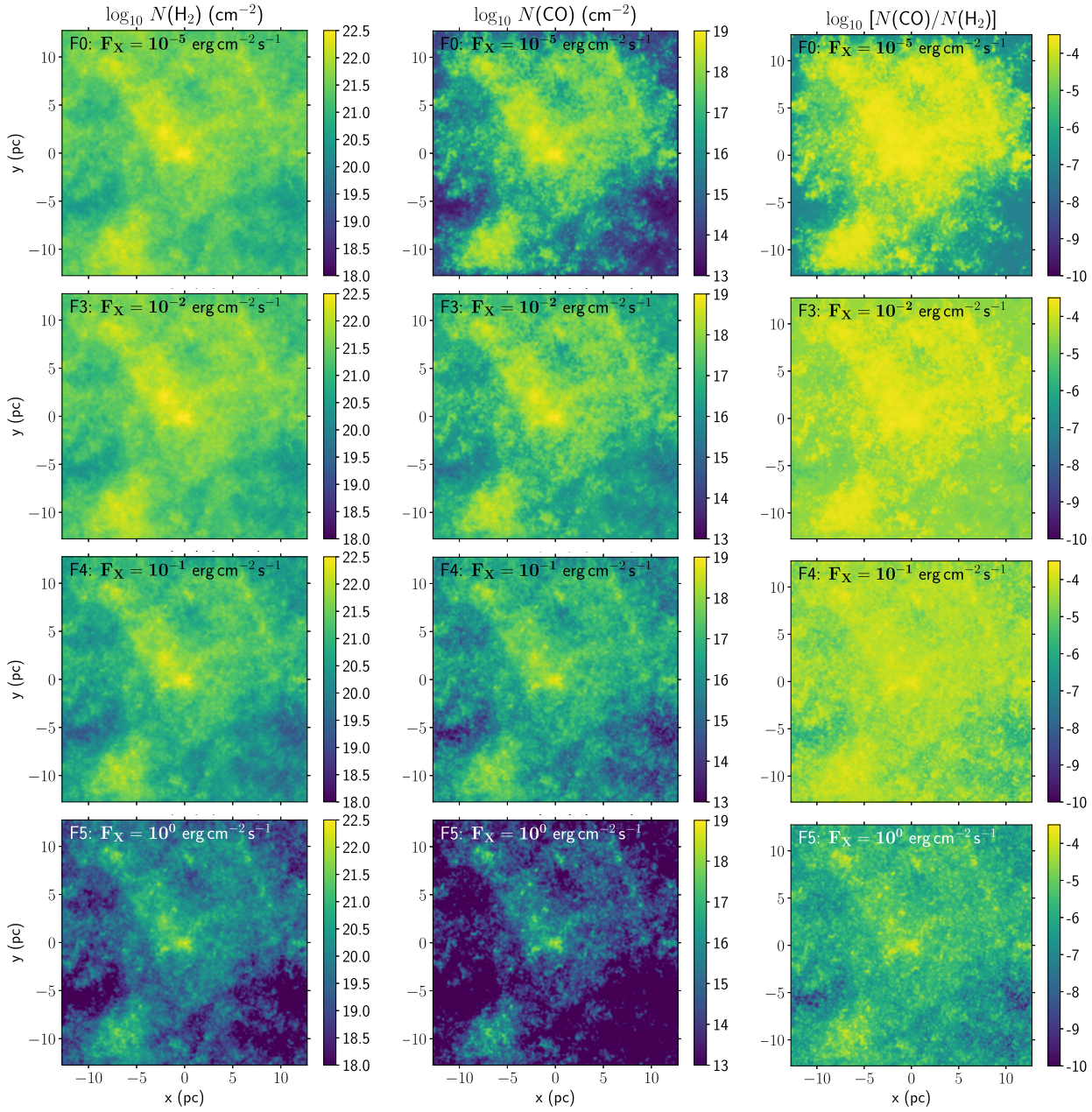

Figure 11. Column density of H_2 (left), CO (centre), and the column-density ratio $N(CO)/N(H_2)$ (right), for the fractal cloud irradiated with an external X-ray radiation field of 10^{-5} erg cm^{-2} s^{-1} (thermal spectrum, $kT = 1$ keV) (run F0; top row), 10^{-2} erg cm^{-2} s^{-1} (run F3; 2nd row), 10^{-1} erg cm^{-2} s^{-1} (run F4; 3rd row), and 1 erg cm^{-2} s^{-1} (run F5; bottom row) for 4 Myr. CO is more effectively destroyed by the incident X-ray field than H_2, leading to a decreasing CO-to-H_2 ratio with increasing $4\pi J_X$.

reaction (#34) become the main one, by which stage most CO is already destroyed.

For CR ionization of molecular clouds, Bisbas et al. (2015) found that He^+ is the main destruction agent of CO, which superficially appears in conflict with our result. The resolution to this seems to be that at late times in our flare simulation He^+ is the main destruction channel, but most of the CO has already been destroyed through other reaction channels by the time He^+ becomes important. This highlights an important difference between equilibrium and non-equilibrium chemistry.

We do assume that the rotational temperature of CO molecules (which is what determines the UV dissociation rate) is the same as the kinetic temperature. In fact the rotational temperature lags behind rapid changes in the kinetic temperature, but the time-scale is $\ll$1 yr for the gas densities in the cloud that we simulate.

The reason H_2 is so much more robust than other molecular species is that it is not destroyed by the FUV radiation that the non-thermal electrons excite. Indeed the excitation of H_2 molecules is the main source of this locally generated FUV field. Once the H^+ mass fraction increases to the point that the electron fraction reaches $\sim$0.1, most of the absorbed X-ray energy goes into Coulomb heating (Dalgarno et al. 1999) and the gas temperature rises above 10^3 K in most of the cloud mass. The rate of collisional dissociation of H_2 from collisions with H atoms increases hugely from $T =$

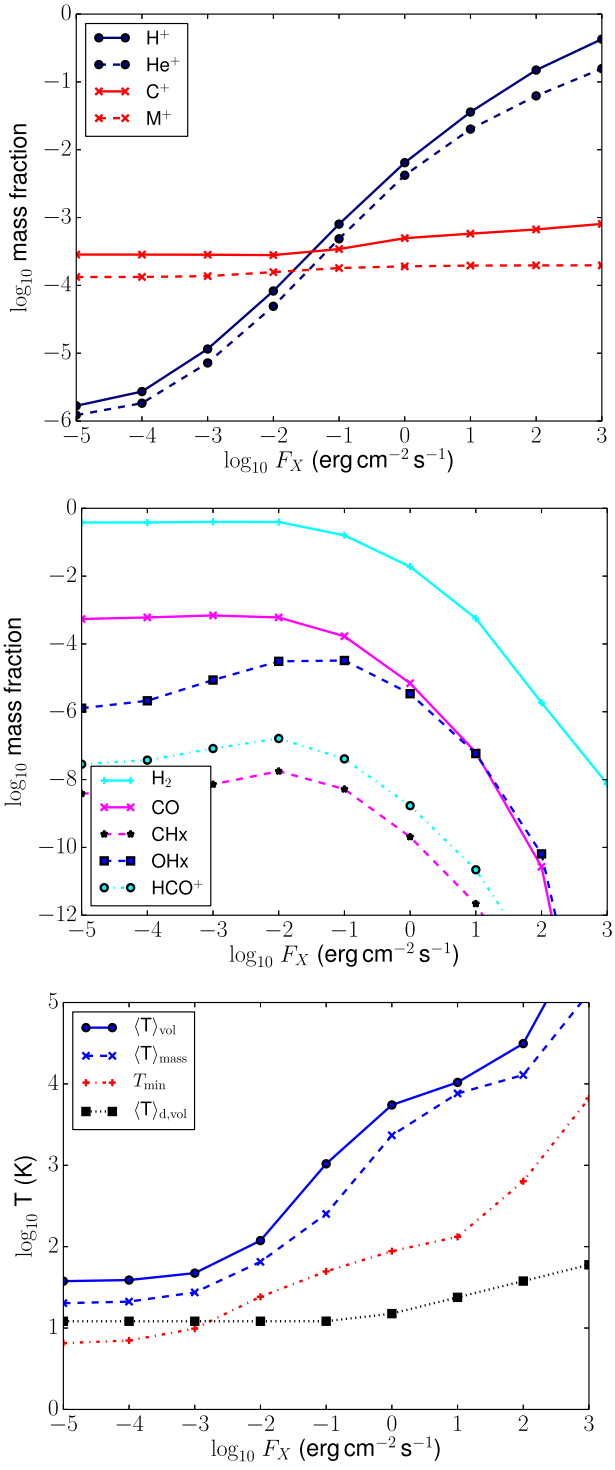

Figure 12. Change in the mass fraction of ionic species (top panel), molecular species (middle panel), and temperature evolution (bottom panel) as a function of the incident X-ray flux on a fractal molecular cloud. These are the mass fractions of all gas in the simulation domain, after 4×10^6 yr of evolution to chemical equilibrium. The volume-weighted ($\langle T \rangle_{\rm vol}$) and mass-weighted ($\langle T \rangle_{\rm mass}$) mean temperatures are plotted, together with the minimum gas temperature, $T_{\rm min}$, and volume-weighted mean dust temperature, $\langle T \rangle_{\rm d,\,vol}$.

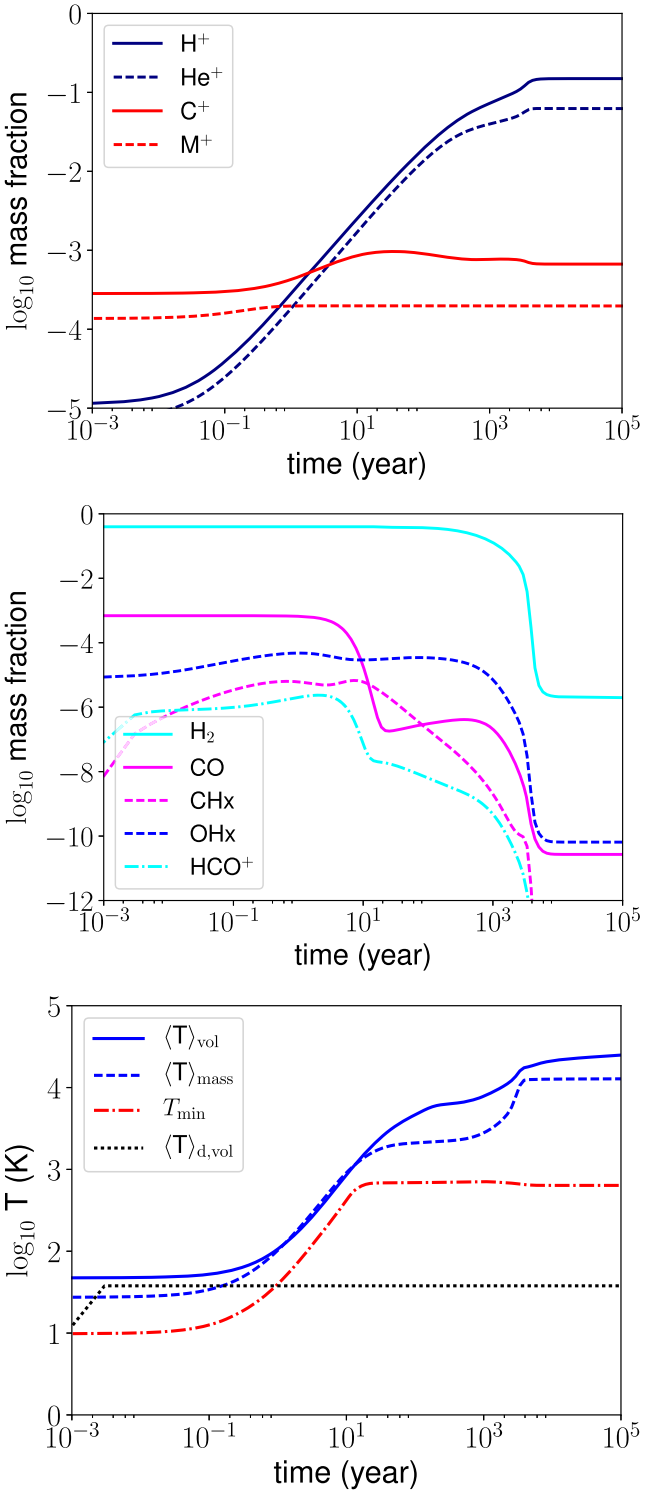

Figure 13. Evolution of the mass fraction of various ionic species (top panel), molecular species (middle panel), and temperature (bottom panel) over time, measured from when the X-ray flux is increased by a factor of 10^5. The volume-weighted ($\langle T \rangle_{\rm vol}$) and mass-weighted ($\langle T \rangle_{\rm mass}$) mean temperatures are plotted in the bottom panel, together with the minimum gas temperature, $T_{\rm min}$, and volume-weighted mean dust temperature, $\langle T \rangle_{\rm d,\,vol}$.

1000 to $T = 5000$ K, and this is what ultimately destroys the H_2. When the H_2 mass fraction decreases, this reduces the cooling rate and the temperature increases, further decreasing the H_2 fraction in a runaway process until a new equilibrium temperature is reached.

5.2 Relaxation once the flare switches off

We now consider what happens if the increased X-ray irradiation switches off after a certain time; here we take 1, 10, 25, and 100 yr as examples. We restart from the flare simulation of the previous subsection but decrease the X-ray irradiation to $4\pi J_X = 10^{-3}$ erg cm^{-2} s^{-1} (model F2). This decrease is again instantaneous, and takes effect everywhere in the domain because of the infinite-speed-of-light approximation. The gas then cools and molecules reform. The global evolution of the ions and molecules is plotted for these three flare durations in Fig. 14, where the top panel shows the results of the 1 yr flare, the middle panel the 10 yr flare, and the bottom panel depicts the results of the 25 yr flare.

If the duration of the flare is only 1 yr, then the gas temperature has not increased dramatically and the molecular species have not been significantly affected by the X-rays (see also bottom panel of Fig. 13), and so not too much changes after the flare is switched off. Fig. 13 shows that most of the CO and HCO^+ are already destroyed after 10 yr, so for a flare duration of 10 yr or longer we see significant evolution during and after the flare in Fig. 14.

After the flare the ionic mass fractions decrease over 10^2–10^4 yr, and reach equilibrium in about 10^5 yr in all cases. The molecular evolution is somewhat more complicated, but the trend is that CO starts to reform immediately, and is approaching its equilibrium mass fraction after 10^5 yr. For shorter flares the recovery is faster: for a 10 yr flare the CO mass fractions reaches half of its pre-flare equilibrium value after 1750 yr; for a 25 yr flare it takes 4000 ys; and for the 100 yr flare (not shown) 31 000 yr. H_2 remains constant because it was not destroyed by the flare. This result raises the possibility that molecular clouds with negligible CO abundance may exist near X-ray sources simply because X-ray flares efficiently destroy CO but not H_2. Since it takes 10^3–10^5 yr to reform the CO, we expect that molecular clouds near centres of galaxies that are occasionally active, and clouds hosting young massive star clusters with X-ray binaries, can have out-of-equilibrium CO-to-H_2 ratios for much of their lifetime (see Section 6).

6 DISCUSSION

We have shown that a gas cloud exposed to an X-ray flare with radiation energy density of $E_{\rm rad} \sim 3 \times 10^{-9}$ erg cm^{-3} will suffer catastrophic CO destruction for flares of duration 10 yr or longer, and that the flare duration must be $\gtrsim$1000 yr to significantly destroy the H_2. Also, gas clouds irradiated by a constant X-ray energy density $E_{\rm rad} \gtrsim 3 \times 10^{-13}$ erg cm^{-3} (F3) show significant heating and chemical effects, and X-rays dominate over CRs as the main heating agent (assuming the CR flux does not scale with X-ray flux). If $E_{\rm rad} \gtrsim 3 \times 10^{-12}$ erg cm^{-3} (F4) then X-rays begin to significantly destroy CO and H_2. It is useful to discuss where such conditions arise, ignoring for now the issue of attenuation and focusing purely on the dilution due to the inverse-square law. The energy density at a distance d from a point source with luminosity $L_{\rm x}$ is given by

$$E_{\rm rad} = \frac{L_{\rm x}}{4\pi c d^2} = 2.8 \times 10^{-9} \frac{L_{\rm x}}{10^{40}\ {\rm erg\ s^{-1}}} \left(\frac{1\ {\rm pc}}{d}\right)^2 {\rm erg\ cm^{-3}}. \quad (18)$$

The Galactic Centre today has an X-ray luminosity of $L_{\rm x} \lesssim 10^{35}$ erg s^{-1}, implying that only clouds within a small fraction of a parsec have significant CO depletion from the current X-ray emission of Sgr A*. During the flare from 100 yr ago, the luminosity was 4 orders of magnitude larger, but still only clouds within $\lesssim$0.5 pc of Sgr A* would have been affected as strongly as the cloud we simulate. Our results for the simulations with X-ray fields of differing strength show that clouds close to Sgr A* (0.5–10 pc) would have some CO destruction, with the effect decreasing with distance. For $d \gtrsim 10$ pc ($E_{\rm rad} \lesssim 3 \times 10^{-12}$ erg cm^{-3}, comparable to simulation F4 or weaker) the CO abundance should actually be enhanced because of the X-ray heating and production of free electrons. Our results imply that the clouds in the circumnuclear disc around Sgr A* could have been significantly affected by X-rays, but the clouds in the 100-pc molecular ring would have remained largely unaffected, given the luminosity estimates of the flare obtained from X-ray reflection (Ponti et al. 2010).

AGN can have $L_{\rm x} > 10^{43}$ erg s^{-1}, for which gas clouds up to 30 pc (larger for higher $L_{\rm x}$) from the black hole should have their CO completely destroyed by X-ray radiation, unless they are optically thick to hard X-rays. CO should be depleted out to $d \gtrsim 1000$ pc, and for sources that emit with this luminosity for thousands of years the H_2 should also be depleted, again with stronger depletion closer to the source.

The class of ultraluminous X-ray sources (ULX) have $L_{\rm x} \sim 10^{39}$–10^{42} erg s^{-1} (Swartz et al. 2004), and it is thought that some of these are powered by pulsars, stellar-mass black holes, and possibly intermediate-mass black holes for the most luminous of them (Mezcua et al. 2013; Bachetti 2016; Earnshaw et al. 2016; Mezcua et al. 2016). The pulsars and stellar-mass black holes are associated with high-mass star formation, and hence with molecular clouds. This, together with the variable nature of ULX sources (Bachetti 2016) suggest that we should see strong effects of X-rays on the chemistry and temperature of molecular clouds in the vicinity of ULX, out to tens of parsecs from the source. For the most luminous ULXs, this radius is 300–1000 pc, a significant fraction of the volume of a dwarf galaxy.

Fig. 12 shows that simulation F3, with $E_{\rm rad} \sim 3 \times 10^{-13}$ erg cm^{-3} (Table 7), divides the lower flux simulations where X-rays have little effect, from the high-flux simulations where X-rays have a big impact on the chemistry and thermal state of the molecular cloud. This is a few times less than the energy density of the ISM in the Galactic plane in CRs, magnetic fields, and turbulent kinetic energy ($\sim$1 eV cm^{-3}; Cox 2005). Our results imply, therefore, that X-rays will dominate the chemistry/thermodynamics of molecular clouds if the X-ray energy density is comparable to or exceeds that of CRs. This claim is of course dependent on energy and environment, because the interaction cross-sections of both X-rays and CRs are strongly energy dependent. Furthermore, sources of CRs are invariably also sources of X-rays, but the scaling of energy density with respect to distance from the source is not the same for CRs and X-rays, because CRs diffuse whereas X-rays stream freely until they are absorbed. Absorption cross-sections of CRs are very uncertain, but it should still be possible to use the code we have developed to constrain the conditions under which X-rays deposit more energy in molecular clouds than CRs, and vice versa.

The local far-UV ISRF has $E_{\rm FUV} \sim 5 \times 10^{-14}$ erg cm^{-3} (Draine 1978) (or $4\pi J_{\rm FUV} \approx 1.5 \times 10^{-3}$ erg cm^{-2} s^{-1}) which is significantly smaller than the ISM energy density in CRs and the X-ray energy density in simulation F4. The ISRF can significantly affect ISM chemistry with a smaller energy density than X-rays (or CRs)

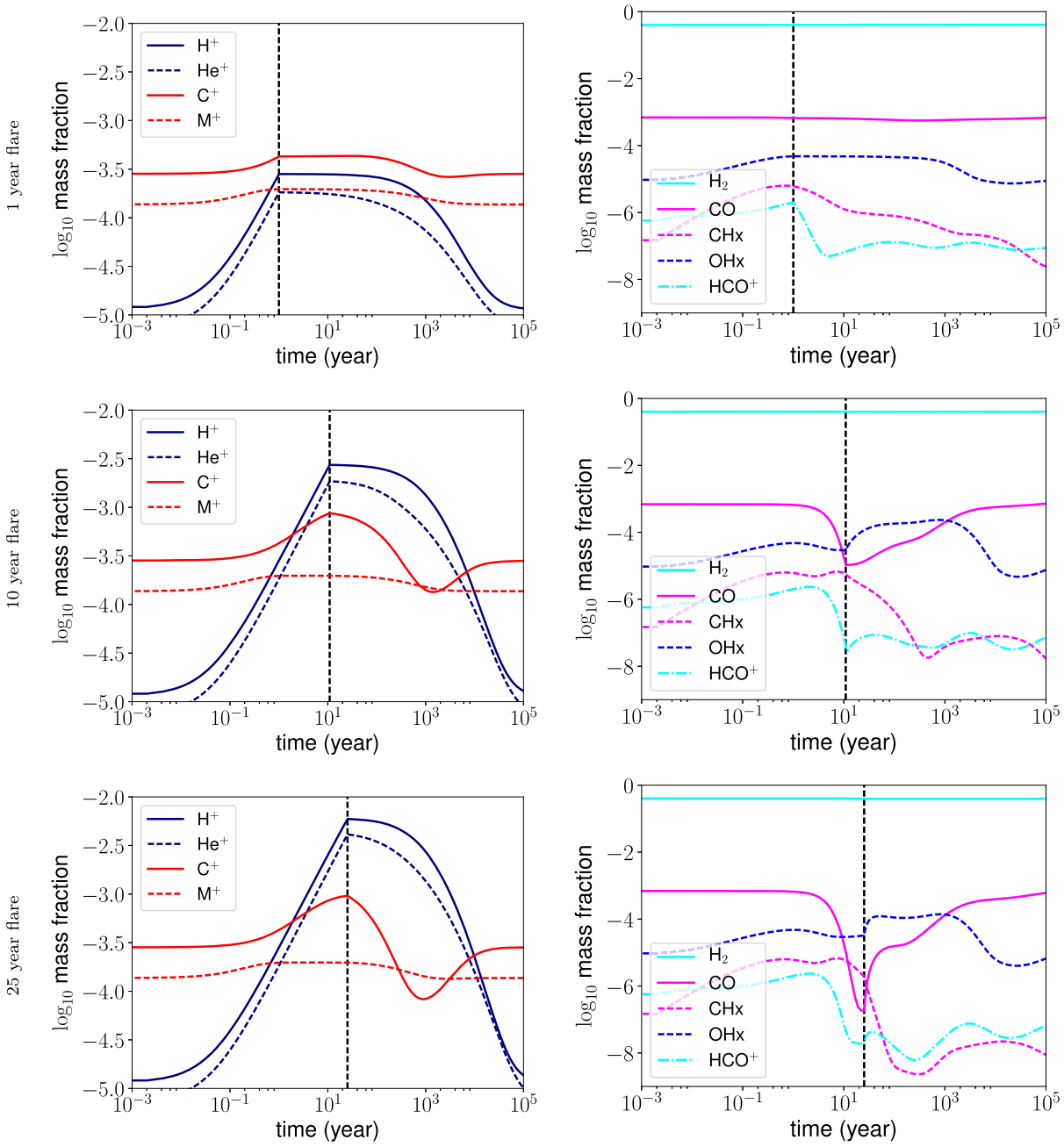

Figure 14. Evolution of the total mass fractions of various ionic species (left column) and molecular species (right column) over time, measured from when the X-ray flare is switched on, for the case where the flare duration was 1 (top row), 10 (middle row), and 25 yr (bottom row). The vertical line shows when the flare was switched off in each simulation. While H_2 is largely unaffected, CO is effectively destroyed by the X-ray flare if it lasts for 10 yr or longer.

because it has a larger absorption cross-section, and so a larger heating rate per unit energy density, but it consequently can only affect the outer (low-extinction) layers of a molecular cloud (cf. Meijerink & Spaans 2005). Fig. 8 shows that the low-extinction part of the cloud is only significantly affected by the X-rays for simulations F3 and above, with $E_{\rm rad} \gtrsim 3.3 \times 10^{-13}\,{\rm erg\,cm^{-3}}$. This reflects that only a small fraction of the X-ray radiation is absorbed in the low-extinction part of the cloud, so the X-rays must have a significantly larger energy density than FUV in order to have a comparable effect at low column densities. In contrast, the high-extinction part of the cloud is already heated by X-rays for a flux 10 times lower (F2) because (i) here it is not competing with the FUV but only with CRs, and (ii) the majority of the X-ray radiation is deposited here.

Our 1D test calculations in Section 3.1 showed that H_2 is a significant coolant when dense clouds are strongly irradiated by X-rays, supported by the CLOUDY calculations in Section 3.2. The 3D simulations of an X-ray flare show (see Fig. 13) that molecular gas is heated to $T \sim 10^3\,{\rm K}$ in about 10 yr, into the temperature regime where H_2 cooling becomes effective. We therefore expect that this hot H_2 gas would emit in the infrared and be observable with upcoming observatories such as the *James Webb Space Telescope*

(Gardner et al. 2006; Kalirai 2018). Our simulations predict that CO is destroyed on a similar (10–20 yr) time-scale to gas heating, and so it should be possible to observe CO emission decreasing on the same time-scale as H_2 emission switches on after a bright flare near a molecular cloud.

Glover & Mac Low (2007b) showed that turbulent motions in molecular clouds can significantly speed up the formation of H_2 and other molecules. We cannot address this with the static simulations presented here, but future calculations with a turbulent cloud will study whether CO can re-form more quickly than indicated by our results.

Our results should also have application to protoplanetary discs, where Cleeves et al. (2017) showed that time-dependent X-ray irradiation can modify the observable HCO^+ signature in the disc. Low-mass protostars typically have strong X-ray emission and variability on account of the strong surface magnetic fields, and this radiation field strongly affects the properties of protostellar discs (Glassgold, Najita & Igea 1997). The time-dependent effects of the X-ray irradiation have not yet been investigated in great detail.

A limitation of our work is that we use the infinite speed-of-light approximation, whereas the chemical and thermal properties of the molecular cloud that we model are changing on a time-scale less than the light traveltime across the cloud for the model of an X-ray flare. If we tracked the photon front propagating through a cloud then the heating, dissociation, and ionization would sweep through the cloud rather than happen simultaneously at all places. The same chemical and thermal evolution would still occur, but there would be time offsets between different parts of the cloud depending on when they were first exposed to the X-ray flare. How this would appear to an observer is very dependent on the angle between the photon propagation direction and the observer's line of sight. If the photon front were propagating directly towards the observer then nothing would look different, whereas if it were propagating at right angles then we could potentially see different molecular and atomic transitions switch on and off in a wave moving across a cloud as more of the cloud gets heated by X-rays. The long-term evolution of the cloud, which is perhaps the most interesting result we have obtained, would not look any different because the time-scales for recombination and for CO to re-form are much longer than the light-crossing time of a cloud.

7 CONCLUSIONS

This paper presents a new implementation of hydrogen and carbon non-equilibrium chemistry when exposed to a (potentially time-varying) X-ray radiation field. The chemical network is relatively small, so that it can be integrated efficiently enough for use in 3D magnetohydrodynamic simulations of molecular clouds and the ISM. Comparison of 1D test calculations using the new network and more complex XDR/PDR codes such as CLOUDY shows that the gas temperature and abundances of the most abundant species agree satisfactorily. Species with typically low abundance, namely CH_x, OH_x, and HCO^+, show poor agreement with CLOUDY, probably reflecting their status in our network as *helper molecules* whose main purpose is to obtain the correct abundances of C^+, C, and CO. The chemical network is coupled to the TREERAY/OPTICAL DEPTH solver (Wünsch et al. 2018) for radiative transfer of the far-UV ISRF, modified to include X-ray radiative transfer, and implemented in the simulation code FLASH.

The first application of the code was to study the equilibrium chemical and thermal state of a fractal molecular cloud when exposed to X-ray radiation of different intensities. UV radiation acts only on the surface layers of a molecular cloud, but hard X-rays can penetrate deep into the whole volume of the simulated cloud, and so have a much stronger effect. X-ray energy densities of 3×10^{-16}–3×10^{-14} erg cm^{-3} had limited effects on the cloud other than a small increase in the minimum temperature and also an increase in the CO to H_2 ratio (on account of the increased ion and electron abundances induced by the X-rays). A radiation field with $E_{\rm rad} = 3 \times 10^{-13}$ erg cm^{-3} increased the mean cloud temperature to nearly 100 K, and provided sufficient ionizations that H^+ and He^+ became the main source of electrons (instead of C^+ and M^+, which have much lower overall abundance). The CO abundance for this X-ray radiation field is elevated compared with a zero flux case because of the increased electron abundance. Still stronger radiation fields increased the mean temperature to 10^3–10^4 K or above, and the ionized fractions of H and He to 10 per cent or more.

For weak X-ray irradiation the gas temperature and molecular abundances are strongly correlated with the local extinction at a given point in the cloud because the UV radiation field is stronger than the X-ray field. For stronger irradiation this correlation disappears and the chemical and thermal properties of the gas depend almost entirely on gas density.

We studied the time-dependent response of the fractal cloud to a sudden increase in X-ray radiation intensity for a duration of 1–100 yr, followed by a sudden decrease back to the original intensity. This is a crude model of an X-ray flare from a variable source, such as Sgr A* in the Galactic Centre, or an AGN or ultra-luminous X-ray source. In 1 yr the mass-weighted-mean gas temperature increased from $\sim$30 to $\gtrsim 10^2$ K, and the ionization fraction of H and He increased by more than an order of magnitude. The abundances of molecular species do not change on this short time-scale, however.

After a flare of 10 yr duration, the gas temperature increased to 10^3 K, and H^+ fraction to $\sim$0.01, and the molecular species start to be affected. The CO abundance decreases by more than an order of magnitude, whereas the H_2 abundance is unchanged. For a flare of 25 yr duration or more, the effects on the cloud are similar, with the temperature and H^+ fraction even larger and the CO almost completely destroyed, but H_2 again unaffected. The temperature increase means that H_2 may become a major coolant in the molecular cloud and should emit brightly in the infrared. It takes hundreds to thousands of years after the flare for the CO to re-form and reach a value close to its pre-flare abundance. The main agent of CO destruction is the locally generated FUV radiation field, produced by H atoms and H_2 molecules that are excited by collisions with high-energy, non-thermal secondary electrons. Only once the CO abundance is already very low does the He^+ destruction channel become important.

As a function of time, the CO-to-H_2 abundance decreases dramatically for flares of duration a few years or more. Our main result is that CO is destroyed almost 100 times more rapidly than H_2, because of the different destruction channels of these molecules. Our results show that some molecular clouds that have been exposed to recent intense X-ray radiation should be still out of chemical equilibrium, and we predict that some of these clouds will still have fully molecular hydrogen, but will contain very little CO. These CO-dark clouds should remain deficient in CO for about 10^3 yr after a flare (depending on gas density, shorter for higher density gas). Depending on the frequency and intensity of X-ray flares, a molecular cloud near a flaring source could be permanently deficient in CO but still be fully molecular as far as hydrogen is concerned.

For Galactic Centre clouds at $\gtrsim$10 pc from Sgr A* the irradiation from the strong X-ray flare about 100 yr ago was not sufficiently strong to destroy CO, and in fact we predict that the CO abundance

may actually have been enhanced by the X-ray irradiation. Only for clouds within a parsec of Sgr A* would significant CO destruction have occurred.

ACKNOWLEDGEMENTS

We are grateful to the referee for very useful comments and suggestions that have improved this paper. We thank B. Godard for a very useful discussion about modelling the X-ray absorption, T. Millar for discussions on the CO dissociation rate in UMIST12, R. Meijerink for discussions on comparison with his results, and E. Pellegrini for suggesting to use CLOUDY for the comparison and providing preliminary results. JM acknowledges funding from a Royal Society-Science Foundation Ireland University Research Fellowship (14/RS-URF/3219). This research was funded by the ERC starting grant No. 679852 'RADFEEDBACK'. We further acknowledge support by the Deutsche Forschungsgemeinschaft via priority program 1573, Physics of the Interstellar Medium. SW thanks the Bonn-Cologne Graduate School, which is funded through the German Excellence Initiative. DS acknowledges funding by the Deutsche Forschungsgemeinschaft (DFG) via the Collaborative Research Center SFB 956 'Conditions and Impact of Star Formation' (subproject C5). SCOG acknowledges support from the Deutsche Forschungsgemeinschaft via SFB 881, 'The Milky Way System' (sub-projects B1, B2, and B8), and from the European Research Council under the European Community's Seventh Framework Programme (FP7/2007 - 2013) via the ERC Advanced Grant 'STARLIGHT: Formation of the First Stars' (project number 339177). RW acknowledges support by the Albert Einstein Centre for Gravitation and Astrophysics via the Czech Science Foundation grant 14-37086G and by the institutional project RVO:67985815 of the Academy of Sciences of the Czech Republic. The authors acknowledge the DJEI/DES/SFI/HEA Irish Centre for High-End Computing (ICHEC) for the provision of computational facilities and support. The software used in this work was in part developed by the DOE-supported ASC/Alliance Center for Astrophysical Thermonuclear Flashes at the University of Chicago. This research has made use of NASA's Astrophysics Data System.

REFERENCES

Abel T., Anninos P., Zhang Y., Norman M. L., 1997, New Astron., 2, 181
Abrahamsson E., Krems R. V., Dalgarno A., 2007, ApJ, 654, 1171
Ackermann M. et al., 2011, ApJ, 743, 171
Aharonian F. A., 2013, Astropart. Phys., 43, 71
Asplund M., Grevesse N., Sauval A. J., Scott P., 2009, ARA&A, 47, 481
Bachetti M., 2016, Astron. Nachr., 337, 349
Baczynski C., Glover S. C. O., Klessen R. S., 2015, MNRAS, 454, 380
Badnell N. R. et al., 2003, A&A, 406, 1151
Badnell N. R., 2006, ApJS, 167, 334
Bakes E. L. O., Tielens A. G. G. M., 1994, ApJ, 427, 822
Barlow S. E., 1984, PhD thesis, University of Colorado at Boulder
Barnes J., Hut P., 1986, Nature, 324, 446
Bell K. L., Berrington K. A., Thomas M. R. J., 1998, MNRAS, 293, L83
Bisbas T. G., Papadopoulos P. P., Viti S., 2015, ApJ, 803, 37
Bisbas T. G., van Dishoeck E. F., Papadopoulos P. P., Szűcs L., Bialy S., Zhang Z.-Y., 2017, ApJ, 839, 90
Black J. H., 1981, MNRAS, 197, 553
Black J. H., Dalgarno A., 1977, ApJS, 34, 405
Brian J., Mitchell A., 1990, Phys. Rep., 186, 215
Brown P. N., Byrne G. D., Hindmarsh A. C., 1989, SIAM J. Sci. Stat. Comput., 10, 1038ff
Burton M. G., Hollenbach D. J., Tielens A. G. G. M., 1990, ApJ, 365, 620
Carty D., Goddard A., Köhler S. P. K., Sims I. R., Smith I. W. M., 2006, J. Phys. Chem. A, 110, 3101
Caselli P., Walmsley C. M., Terzieva R., Herbst E., 1998, ApJ, 499, 234
Cen R., 1992, ApJS, 78, 341
Churazov E., Khabibullin I., Sunyaev R., Ponti G., 2017a, MNRAS, 465, 45
Churazov E., Khabibullin I., Ponti G., Sunyaev R., 2017b, MNRAS, 468, 165
Churazov E., Khabibullin I., Sunyaev R., Ponti G., 2017c, MNRAS, 471, 3293
Clark P. C., Glover S. C. O., Klessen R. S., 2012, MNRAS, 420, 745
Clark P. C., Glover S. C. O., Ragan S. E., Shetty R., Klessen R. S., 2013, ApJ, 768, L34
Cleeves L. I., Bergin E. A., Öberg K. I., Andrews S., Wilner D., Loomis R., 2017, ApJ, 843, L3
Cox D. P., 2005, ARA&A, 43, 337
Dalgarno A., McCray R. A., 1972, ARA&A, 10, 375
Dalgarno A., Yan M., Liu W., 1999, ApJS, 125, 237
de Avillez M. A., Breitschwerdt D., 2012a, ApJ, 756, L3
de Avillez M. A., Breitschwerdt D., 2012b, ApJ, 756, L3
de Ruette N., Miller K. A., O'Connor A. P., Urbain X., Buzard C. F., Vissapragada S., Savin D. W., 2016, ApJ, 816, 31
Draine B. T., 1978, ApJS, 36, 595
Dufton P. L., Kingston A. E., 1991, MNRAS, 248, 827
Earnshaw H. M. et al., 2016, MNRAS, 456, 3840
Ferland G. J. et al., 2013, Rev. Mex. Astron. Astrofis., 49, 137
Ferland G. J. et al., 2017, Rev. Mex. Astron. Astrofis., 53, 385
Ferland G. J., Peterson B. M., Horne K., Welsh W. F., Nahar S. N., 1992, ApJ, 387, 95
Flower D. R., 2001, J. Phys. B At. Mol. Phys., 34, 2731
Flower D. R., Launay J. M., 1977, J. Phys. B At. Mol. Phys., 10, 3673
Fryxell B. et al., 2000, ApJS, 131, 273
Gardner J. P. et al., 2006, Space Sci. Rev., 123, 485
Gatto A. et al., 2017, MNRAS, 466, 1903
Girichidis P. et al., 2016, MNRAS, 456, 3432
Glassgold A. E., Najita J., Igea J., 1997, ApJ, 480, 344
Glover S. C. O., 2003, ApJ, 584, 331
Glover S. C. O., Abel T., 2008, MNRAS, 388, 1627
Glover S. C. O., Clark P. C., 2012, MNRAS, 421, 116
Glover S. C. O., Jappsen A.-K., 2007, ApJ, 666, 1
Glover S. C. O., Mac Low M.-M., 2007a, ApJS, 169, 239
Glover S. C. O., Mac Low M.-M., 2007b, ApJ, 659, 1317
Glover S. C. O., Savin D. W., 2009, MNRAS, 393, 911
Glover S. C. O., Federrath C., Mac Low M.-M., Klessen R. S., 2010, MNRAS, 404, 2
Gnat O., Ferland G. J., 2012, ApJS, 199, 20
Goldsmith P. F., Langer W. D., 1978, ApJ, 222, 881
Gong M., Ostriker E. C., Wolfire M. G., 2017, ApJ, 843, 38
Górski K. M., Hivon E., Banday A. J., Wandelt B. D., Hansen F. K., Reinecke M., Bartelmann M., 2005, ApJ, 622, 759
Gredel R., Lepp S., Dalgarno A., 1987, ApJ, 323, L137
Gredel R., Lepp S., Dalgarno A., Herbst E., 1989, ApJ, 347, 289
H. E. S. S. Collaboration, 2017, ApJ, 850, L22
Heays A. N., Bosman A. D., van Dishoeck E. F., 2017, A&A, 602, A105
Hocuk S., Spaans M., 2010, A&A, 522, A24
Hollenbach D., McKee C. F., 1979, ApJS, 41, 555
Hollenbach D., McKee C. F., 1989, ApJ, 342, 306
Hummer D. G., Storey P. J., 1998, MNRAS, 297, 1073
Johnson C. T., Burke P. G., Kingston A. E., 1987, J. Phys. B At. Mol. Phys., 20, 2553
Kalirai J., 2018, Contemp. Phys., 59, 251
Karpas Z., Anicich V., Huntress W. T., 1979, J. Chem. Phys., 70, 2877
Keenan F. P., Lennon D. J., Johnson C. T., Kingston A. E., 1986, MNRAS, 220, 571
Kim J. K., Theard L. P., Huntress W. T., Jr, 1975, Chem. Phys. Lett., 32, 610
Koyama K., Maeda Y., Sonobe T., Takeshima T., Tanaka Y., Yamauchi S., 1996, PASJ, 48, 249
Krivonos R. et al., 2017, MNRAS, 468, 2822
Lepp S., Dalgarno A., 1996, A&A, 306, L21

Lepp S., McCray R., 1983, ApJ, 269, 560
Lepp S., Shull J. M., 1983, ApJ, 270, 578
Liszt H., 2003, A&A, 398, 621
Mac Low M.-M., Shull J. M., 1986, ApJ, 302, 585
Mackey J., Lim A. J., 2010, MNRAS, 403, 714
Maloney P. R., Hollenbach D. J., Tielens A. G. G. M., 1996, ApJ, 466, 561
Martin P. G., Schwarz D. H., Mandy M. E., 1996, ApJ, 461, 265
Martin P. G., Keogh W. J., Mandy M. E., 1998, ApJ, 499, 793
Mathis J. S., Rumpl W., Nordsieck K. H., 1977, ApJ, 217, 425
McCall B. J. et al., 2004, Phys. Rev. A, 70, 052716
McElroy D., Walsh C., Markwick A. J., Cordiner M. A., Smith K., Millar T. J., 2013, A&A, 550, A36
Meijerink R., Spaans M., 2005, A&A, 436, 397
Meijerink R., Spaans M., Israel F. P., 2006, ApJ, 650, L103
Meijerink R., Spaans M., Loenen A. F., van der Werf P. P., 2011, A&A, 525, A119
Mezcua M., Roberts T. P., Sutton A. D., Lobanov A. P., 2013, MNRAS, 436, 3128
Mezcua M., Civano F., Fabbiano G., Miyaji T., Marchesi S., 2016, ApJ, 817, 20
Micic M., Glover S. C. O., Federrath C., Klessen R. S., 2012, MNRAS, 421, 2531
Mills E. A. C., Güsten R., Requena-Torres M. A., Morris M. R., 2013, ApJ, 779, 47
Molaro M., Khatri R., Sunyaev R. A., 2016, A&A, 589, A88
Morrison R., McCammon D., 1983, ApJ, 270, 119
Moser L. et al., 2017, A&A, 603, A68
Nelson R. P., Langer W. D., 1997, ApJ, 482, 796
Nelson R. P., Langer W. D., 1999, ApJ, 524, 923
Neufeld D. A., Kaufman M. J., 1993, ApJ, 418, 263
Neufeld D. A., Lepp S., Melnick G. J., 1995, ApJS, 100, 132
Odaka H., Aharonian F., Watanabe S., Tanaka Y., Khangulyan D., Takahashi T., 2011, ApJ, 740, 103
Osterbrock D. E., 1989, Astrophysics of Gaseous Nebulae and Active Galactic Nuclei. University Science Books, Mill Valley, CA
Palla F., Salpeter E. E., Stahler S. W., 1983, ApJ, 271, 632
Panoglou D., Cabrit S., Pineau Des Forêts G., Garcia P. J. V., Ferreira J., Casse F., 2012, A&A, 538, A2
Pequignot D., 1990, A&A, 231, 499
Pequignot D., 1996, A&A, 313, 1026
Peters T. et al., 2017, MNRAS, 466, 3293
Petuchowski S. J., Dwek E., Allen J. E., Jr., Nuth J. A., III, 1989, ApJ, 342, 406
Pfrommer C., Pakmor R., Schaal K., Simpson C. M., Springel V., 2017, MNRAS, 465, 4500
Ponti G. et al., 2015, MNRAS, 453, 172
Ponti G., Terrier R., Goldwurm A., Belanger G., Trap G., 2010, ApJ, 714, 732
Prasad S. S., Huntress W. T., Jr., 1980, ApJS, 43, 1
Prasad S. S., Tarafdar S. P., 1983, ApJ, 267, 603
Punsly B., Rodriguez J., 2013, ApJ, 764, 173
Röllig M. et al., 2007, A&A, 467, 187
Roueff E., 1990, A&A, 234, 567
Roueff E., Le Bourlot J., 1990, A&A, 236, 515
Savin D. W., Krstić P. S., Haiman Z., Stancil P. C., 2004, ApJ, 606, L167
Schauer M. M., Jefferts S. R., Barlow S. E., Dunn G. H., 1989, J. Chem. Phys., 91, 4593
Schroder K., Staemmler V., Smith M. D., Flower D. R., Jaquet R., 1991, J. Phys. B At. Mol. Phys., 24, 2487
Seifried D. et al., 2017, MNRAS, 472, 4797
Shadmehri M., Elmegreen B. G., 2011, MNRAS, 410, 788
Shang H., Glassgold A. E., Shu F. H., Lizano S., 2002, ApJ, 564, 853
Shapiro P. R., Kang H., 1987, ApJ, 318, 32
Shull J. M., van Steenberg M. E., 1985, ApJ, 298, 268
Silva A. I., Viegas S. M., 2002, MNRAS, 329, 135
Spitzer Jr. L., Tomasko M. G., 1968, ApJ, 152, 971
Stancil P. C., Lepp S., Dalgarno A., 1998, ApJ, 509, 1
Stancil P. C., Schultz D. R., Kimura M., Gu J.-P., Hirsch G., Buenker R. J., 1999, A&AS, 140, 225
Stutzki J., Bensch F., Heithausen A., Ossenkopf V., Zielinsky M., 1998, A&A, 336, 697
Sunyaev R., Churazov E., 1998, MNRAS, 297, 1279
Sunyaev R. A., Markevitch M., Pavlinsky M., 1993, ApJ, 407, 606
Swartz D. A., Ghosh K. K., Tennant A. F., Wu K., 2004, ApJS, 154, 519
Tielens A. G. G. M., Hollenbach D., 1985, ApJ, 291, 722
Trevisan C. S., Tennyson J., 2002, Plasma Phys. Control. Fusion, 44, 1263
Vaupré S., Hily-Blant P., Ceccarelli C., Dubus G., Gabici S., Montmerle T., 2014, A&A, 568, A50
Vissapragada S., Buzard C. F., Miller K. A., O'Connor A. P., de Ruette N., Urbain X., Savin D. W., 2016, ApJ, 832, 31
Voronov G. S., 1997, At. Data Nucl. Data Tables, 65, 1
Wakelam V. et al., 2010, Space Sci. Rev., 156, 13
Wakelam V. et al., 2015, ApJS, 217, 20
Walch S. et al., 2015, MNRAS, 454, 238
Walch S. K., Whitworth A. P., Bisbas T., Wünsch R., Hubber D., 2012, MNRAS, 427, 625
Walls M., Chernyakova M., Terrier R., Goldwurm A., 2016, MNRAS, 463, 2893
Weingartner J. C., Draine B. T., 2001, ApJ, 563, 842
Wernli M., Valiron P., Faure A., Wiesenfeld L., Jankowski P., Szalewicz K., 2006, A&A, 446, 367
Wilms J., Allen A., McCray R., 2000, ApJ, 542, 914
Wilson N. J., Bell K. L., 2002, MNRAS, 337, 1027
Wolfire M. G., McKee C. F., Hollenbach D., Tielens A. G. G. M., 2003, ApJ, 587, 278
Woodall J., Agúndez M., Markwick-Kemper A. J., Millar T. J., 2007, A&A, 466, 1197
Wünsch R., Walch S., Dinnbier F., Whitworth A., 2018, MNRAS, 475, 3393
Yan M., 1997, PhD thesis, Harvard University
Zanchet A., Bussery-Honvault B., Jorfi M., Honvault P., 2009, Phys. Chem. Chem. Phys., 11, 6182

SUPPORTING INFORMATION

Supplementary data are available at *MNRAS* online.

cloudy_in.tgz

Please note: Oxford University Press is not responsible for the content or functionality of any supporting materials supplied by the authors. Any queries (other than missing material) should be directed to the corresponding author for the article.

APPENDIX A: CHEMICAL NETWORK

The collisional reactions considered are listed in Table A1 and photo/CR/X-ray reactions in Table A2. The reaction network is a superset of the NL99 Glover & Clark (2012) network, with most additions taken from Gong et al. (2017). The extra reactions included are numbers #13, #14, #15, #18, #25, #28, #29, #31, #39, #40, #41, #56, #60, plus the X-ray photoreactions #62–76.

The results of 1D simulations of the MS05 models 1–4, calculated with and without these additional reactions, are plotted in Figs A1 and A2. The abundances of H_2, CO, H, electrons, and gas temperature are shown in Fig. A1, and abundances of carbon-bearing species in Fig. A2.

The main difference apparent from Fig. A1 is that y(CO) has a very different relationship with column density for the two sets of reactions. The gas temperature is not strongly affected, except for models 2 and 4, which have a strong chemo-thermal instability for the original NL99 network. This is weaker when using the updated network. Looking at the carbon chemistry in Fig. A2, the updated network has consistently lower C^+ abundance for all

Table A1. Collisional reactions used in the new chemical network for modelling X-ray-irradiated gas. GOW17 refers to Gong et al. (2017).

ID	Reaction	Type	Note	Reference
1	$H + e \rightarrow H^+ + 2e$	Collisional ionization	Polynomial fit	Abel et al. (1997)
2	$He + e \rightarrow He^+ + 2e$	Collisional ionization	Not in GOW17	Abel et al. (1997)
3	$C + e \rightarrow C^+ + 2e$	Collisional ionization	Not in GOW17	Voronov (1997)
4	$M + e \rightarrow M^+ + 2e$	Collisional ionization	Not in GOW17	Voronov (1997)
5	$H_2 + e \rightarrow 2H + e$	Collisional dissociation	Not in GOW17	Trevisan & Tennyson (2002)
6	$H_2 + H \rightarrow 3H$	Collisional dissociation	Similar to GOW17	Lepp & Shull (1983), Mac Low & Shull (1986), Martin, Schwarz & Mandy (1996)
7	$H_2 + H_2 \rightarrow H_2 + 2H$	Collisional dissociation	Similar to GOW17	Martin, Keogh & Mandy (1998), Shapiro & Kang (1987), Palla, Salpeter & Stahler 1983
8	$H^+ + e \rightarrow H + \gamma$	Radiative recomb.	Same as GOW17	Ferland et al. (1992)
9	$He^+ + e \rightarrow He + \gamma$	Radiative + dielec. recomb.		Osterbrock (1989), Hummer & Storey (1998), Badnell (2006)
10	$C^+ + e \rightarrow C + \gamma$	Radiative recomb.	Same as GOW17	Badnell et al. (2003), Badnell (2006)
11	$M^+ + e \rightarrow M + \gamma$	Radiative recomb.	Similar to GOW17	Nelson & Langer (1999)
12	$H^+ + e \rightarrow H$	Grain-assisted recomb.	Same as GOW17	Weingartner & Draine (2001)
13	$He^+ + e \rightarrow He$	Grain-assisted recomb.	Same as GOW17	Weingartner & Draine (2001)
14	$C^+ + e \rightarrow C$	Grain-assisted recomb.	Same as GOW17	Weingartner & Draine (2001)
15	$M^+ + e \rightarrow M$	Grain-assisted recomb.	Same as GOW17	Weingartner & Draine (2001)
16	$H + H \rightarrow H_2$	Grain-assisted H_2 form.	Similar to GOW17	Hollenbach & McKee (1979)
17	$H_2^+ + H \rightarrow H_2 + H^+$	Charge ex.	Same as GOW17	Karpas, Anicich & Huntress (1979)
18	$H_2 + H^+ \rightarrow H_2^+ + H$	Charge ex.	Not in GOW17	Savin et al. (2004)
19	$H_3^+ + M \rightarrow M^+ + H_2 + H$	Dissociative charge ex.	Not in GOW17	Nelson & Langer (1999)
20	$H_3^+ + e \rightarrow H_2 + H$	Dissociative recomb.	Same as GOW17	McCall et al. (2004), Woodall et al. (2007)
21	$H_3^+ + C \rightarrow CH_x + H_2$	Formation of CH_x	Same as GOW17	Vissapragada et al. (2016), Gong et al. (2017)
22	$H_3^+ + O \rightarrow OH_x + H_2$	Formation of OH_x	Same as GOW17	de Ruette et al. (2016), Gong et al. (2017)
23	$H_3^+ + O + e \rightarrow O + 3H$	Pseudo-reaction	Same as GOW17	de Ruette et al. (2016), Gong et al. (2017)
24	$H_3^+ + CO \rightarrow HCO^+ + H_2$	Proton transfer	Same as GOW17	Kim, Theard & Huntress (1975)
25	$CH_x + H \rightarrow H_2 + C$	Exchange reaction	Same as GOW17	Wakelam et al. (2010), Gong et al. (2017)
26	$He^+ + H_2 \rightarrow He + H + H^+$	Dissociative charge ex.	Same as GOW17	Schauer et al. (1989)
27	$He^+ + H_2 \rightarrow He + H_2^+$	Charge ex.	Same as GOW17	Barlow (1984)
28	$O^+ + H_2 \rightarrow OH_x + H$	Formation of OH_x	Same as GOW17	Gong et al. (2017)
29	$O^+ + H_2 + e \rightarrow O + 2H$	H_2 destruction	Same as GOW17	Gong et al. (2017)
30	$C^+ + H_2 \rightarrow CH_x + H$	Formation of CH_x	Same as GOW17	Wakelam et al. (2010)
31	$C^+ + H_2 + e \rightarrow C + 2H$	H_2 Destruction	Same as GOW17	Wakelam et al. (2010)
32	$H_2 + H_2^+ \rightarrow H_3^+ + H$	Formation of H_3^+	Same as GOW17	Stancil, Lepp & Dalgarno (1998)
33	$C + H_2 \rightarrow CH_x$	Radiative association	Not in GOW17	Prasad & Huntress (1980)
34	$He^+ + CO \rightarrow He + C^+ + O$	Dissociative charge ex.	GOW17 differs	Petuchowski et al. (1989)
35	$C^+ + OH_x \rightarrow HCO^+$	HCO^+ formation	Same as GOW17	Wakelam et al. (2010)
36	$O + CH_x \rightarrow CO + H$	CO formation	Same as GOW17	Wakelam et al. (2010)
37	$C + OH_x \rightarrow CO + H$	CO formation	Same as GOW17	Zanchet et al. (2009), Wakelam et al. (2010)
38	$HCO^+ + e \rightarrow CO + H$	CO formation	GOW17 rate similar	Brian & Mitchell (1990), McElroy et al. (2013)
39	$OH_x + O \rightarrow 2O + H$	OH_x destruction	Same as GOW17	Carty et al. (2006)
40	$OH_x + He^+ \rightarrow O^+ + He + H$	Dissociative charge ex.	Same as GOW17	Wakelam et al. (2010)
41	$O^+ + H \rightarrow O + H^+$	Charge ex.	Equilibrium	Stancil et al. (1999)
42	$H^+ + O \rightarrow H + O^+$	Charge ex.	Equilibrium	Stancil et al. (1999)
43	$H_2^+ + e \rightarrow 2H$	Dissociative recomb.	Not in GOW17	Abel et al. (1997)

calculations. The original NL99 network produces results much closer to those of MS05; in fact the C^+ abundance showed the largest discrepancy between our results and MS05 in Section 3.1. The neutral C abundance is higher using the updated network except in the region of column density where C^+ and CO co-exist, for which the updated network typically has lower neutral C abundance. At very high column density, the neutral C abundance is much higher with the updated network. CO forms more rapidly with increasing column density using the updated network; this is in much better agreement with the CLOUDY results in Section 3.2.

Table A2. Cosmic-ray, X-ray, and photo-reactions used in the new chemical network. GOW17 refers to Gong et al. (2017).

ID	Reaction	Type	Note	Reference
44	$H_2 + FUV \rightarrow 2H$	Photodiss.	Same as GOW17	Heays et al. (2017)
45	$HCO^+ + FUV \rightarrow CO + H^+$	Photodiss.	Not in GOW17	Heays et al. (2017)
46	$CO + FUV \rightarrow C + O$	Photodiss.	Same as GOW17	Heays et al. (2017)
47	$C + FUV \rightarrow C^+ + e$	Photoioniz.	Same as GOW17	Heays et al. (2017)
48	$M + FUV \rightarrow M^+ + e$	Photoioniz.	Same as GOW17	Heays et al. (2017)
49	$OH_x + FUV \rightarrow O + H$	Photodiss.	Same as GOW17	Heays et al. (2017)
50	$CH_x + FUV \rightarrow C + H$	Photodiss.	Same as GOW17	Heays et al. (2017)
51	$H + CR \rightarrow H^+ + e$	Cosmic-ray ioniz.	$\zeta_H = 3 \times 10^{-17}\ s^{-1}$ per H	Walch et al. (2015)
52	$He + CR \rightarrow He^+ + e$	Cosmic-ray ioniz.	Same as GOW17	Glover et al. (2010)
53	$C + CR \rightarrow C^+ + e$	Cosmic-ray ioniz.	Within 1 per cent of GOW17	Liszt (2003)
54	$H_2 + CR \rightarrow H^+ + H + e$	Cosmic-ray ioniz.	$0.037\zeta_H$ per H_2	Micic et al. (2012)
55	$H_2 + CR \rightarrow 2H$	Cosmic-ray diss.	$0.21\zeta_H$ per H_2	Micic et al. (2012)
56	$H_2 + CR \rightarrow H_2^+ + e$	Cosmic-ray ioniz.	As GOW17; $2\zeta_H$ per H_2	Gong et al. (2017)
57	$CO + CR\ (+ H) \rightarrow HCO^+$	Pseudoreaction, via CO^+	Same as GOW17	Glover et al. (2010)
58	$CO + CR \rightarrow C + O$	Cosmic-ray diss.	$10\zeta_H y(CO)$	Wakelam et al. (2015)
59	$C + CRPHOT \rightarrow C^+ + e$	Ioniz. by CR-induced FUV	Similar to GOW17	Gredel et al. (1987), McElroy et al. (2013)
60	$CO + CRPHOT \rightarrow C + O$	Diss. by CR-induced FUV	GOW17 rate differs	Gredel et al. (1987), McElroy et al. (2013)
61	$M + CRPHOT \rightarrow M^+ + e$	Ioniz. by CR-induced FUV	Similar to GOW17	McElroy et al. (2013) reference Rawlings (1992, private communication)
62	$H + XR \rightarrow H^+ + e$	Secondary ioniz.	Fitted from table	Dalgarno et al. (1999)
63	$He + XR \rightarrow He^+ + e$	Secondary ioniz.	Fitted from table	Dalgarno et al. (1999)
64	$C + XR \rightarrow C^+ + e$	Secondary ioniz.	3.92× rate for H	MS05
65	$M + XR \rightarrow M^+ + e$	Secondary ioniz.	6.67× rate for H	MS05
66	$H_2 + XR \rightarrow H_2^+ + e$	Secondary ioniz.	Fitted from table	Dalgarno et al. (1999)
67	$H_2 + XR \rightarrow 2H$	Secondary diss.	Fitted from table	Dalgarno et al. (1999)
68	$CO + XR \rightarrow C^+ + O + e$	Secondary ioniz.	3.92× rate for H	MS05
69	$CH_x + XR \rightarrow C^+ + H + e$	Secondary ioniz.	3.92× rate for H	MS05
70	$OH_x + XR \rightarrow O + H^+ + e$	Secondary ioniz.	2.97× rate for H	MS05
71	$HCO^+ + XR \rightarrow C^+ + H^+ + O + e$	Secondary ioniz.	3.92× rate for H	MS05
72	$C + XRPHOT \rightarrow C^+ + e$	Ioniz. by XR-induced FUV	Equation (16), Table 3	See Table 3
73	$M + XRPHOT \rightarrow M^+ + e$	Ioniz. by XR-induced FUV	Equation (16), Table 3	See Table 3
74	$CO + XRPHOT \rightarrow C + O$	Ioniz. by XR-induced FUV	Equation (15)	Gredel et al. (1987), McElroy et al. (2013)
75	$CH_x + XRPHOT \rightarrow C + H$	Diss. by XR-induced FUV	Equation (16), Table 3	See Table 3
76	$OH_x + XRPHOT \rightarrow O + H$	Diss. by XR-induced FUV	Equation (16), Table 3	See Table 3

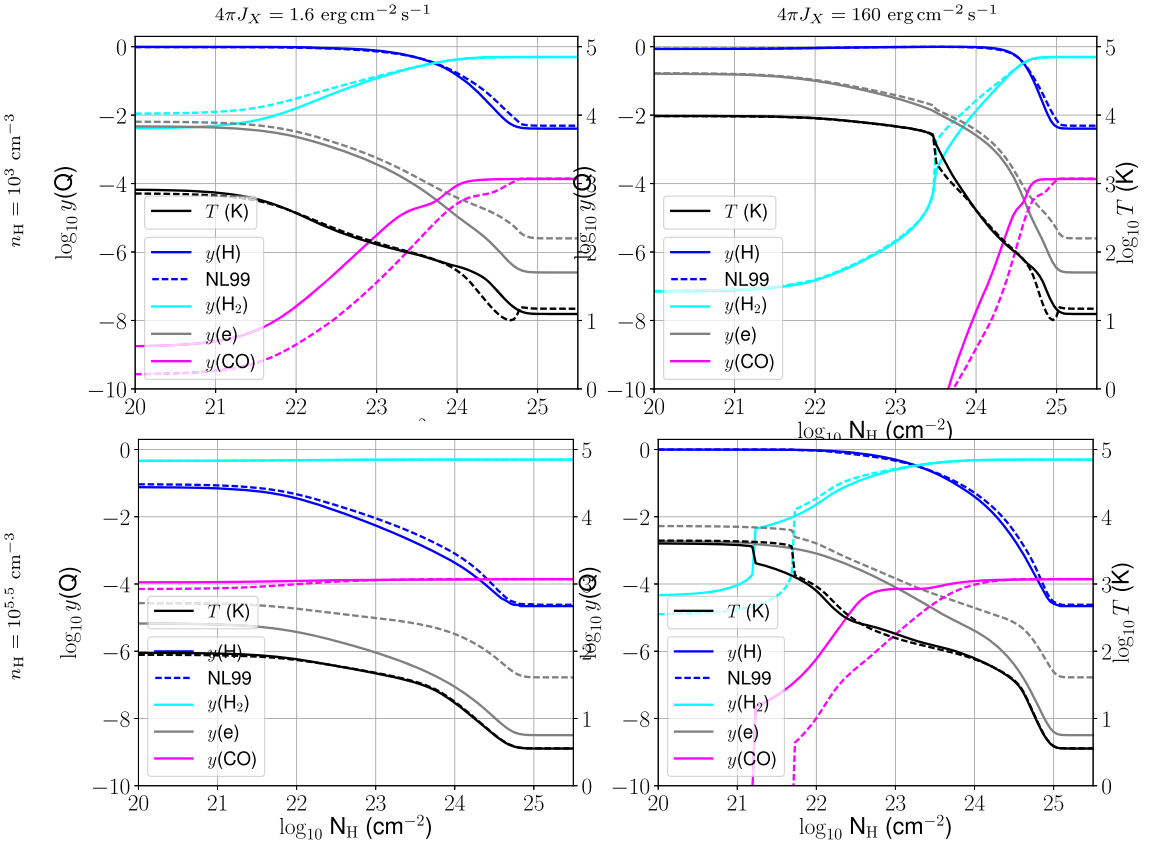

Figure A1. Abundances of H_2, CO, H, electrons, and gas temperature for models 1 (upper left), 2 (upper right), 3 (lower left), and 4 (lower right) calculated using the original NL99 network (dashed lines) and including the Gong et al. (2017) additions (solid lines). The results are plotted as a function of column density of hydrogen. The left-hand vertical axis shows the fractional abundance whereas the right-hand vertical axis shows the temperature scale.

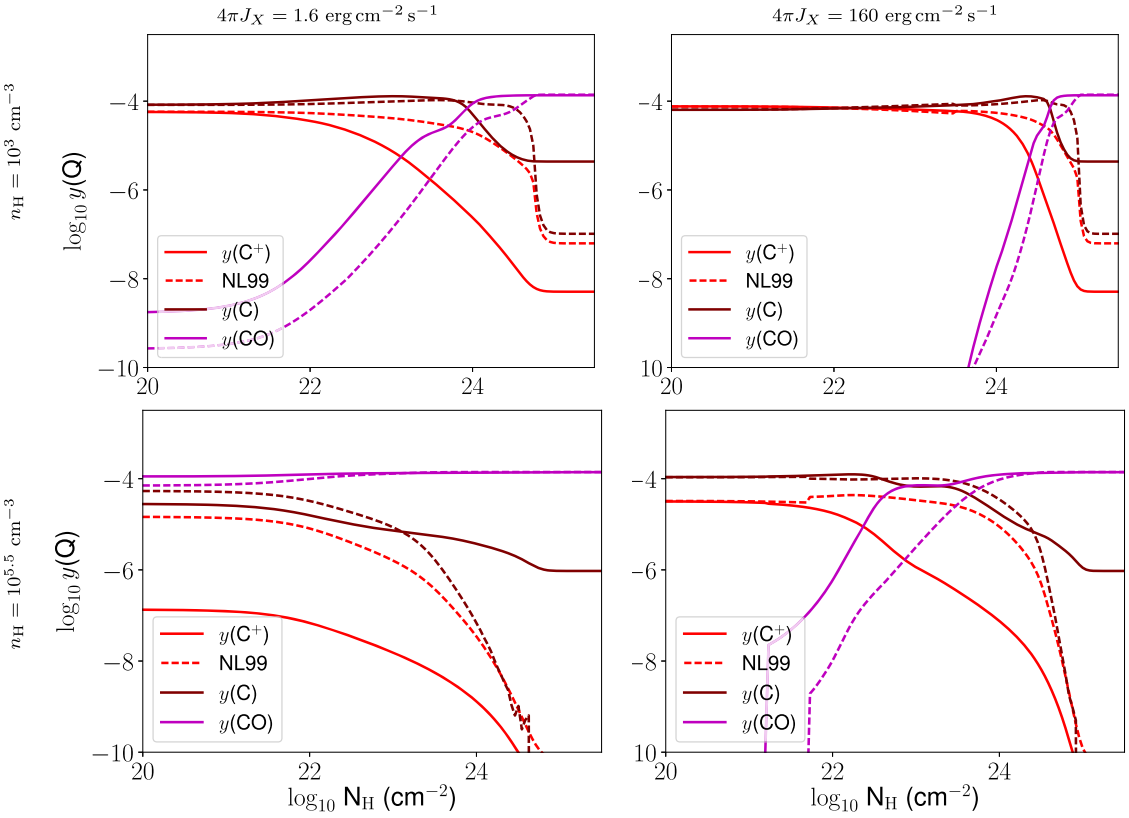

Figure A2. Abundances of carbon-bearing species for models 1 (upper left), 2 (upper right), 3 (lower left), and 4 (lower right) calculated using the original NL99 network (dashed lines) and including the Gong et al. (2017) additions (solid lines). The results are plotted as a function of column density of hydrogen.

APPENDIX B: HEATING AND COOLING RATES

We model the thermal evolution of the gas in our simulations using a cooling function based largely on the one developed by Glover et al. (2010) and Glover & Clark (2012), but updated to account for the effects of X-ray heating, as detailed in Section 2.3 of this paper. A full list of the processes included in the cooling function is given in Table B1, along with the sources for the rates used. For a few processes, we also give additional details below.

Fine structure cooling

We model atomic fine structure cooling from neutral C, O, and Si atoms and C^+ and Si^+ ions by directly solving for the fine structure level populations, with the assumption that the populations of any electronically excited states are zero. This assumption allows us to model C^+ and Si^+ as two-level systems and C, O, and Si as three-level systems, allowing us to write down analytical expressions for the cooling rate from each species in a relatively simple fashion. We do not account for any external sources of radiation other than the cosmic microwave background. The sources for the data used in the level population calculations are listed in Table B1, and a more detailed discussion of our approach can be found in Glover & Jappsen (2007). Note that we use the Si and Si^+ cooling rates as a proxy for the cooling coming from the species represented by M and M^+, which include not only Si but also other low-ionization potential metals such as Mg or Fe. This simplification is somewhat inaccurate, but in practice this is unlikely to be important as the fine structure cooling is typically dominated by C^+ and O in regions with low A_V and by C in regions with high A_V.

CO rovibrational line cooling

We model CO cooling using the cooling tables given in Neufeld & Kaufman (1993) and Neufeld et al. (1995), which are based on a large velocity gradient (LVG) calculation of the CO level populations as a function of the H_2 number density, CO number density temperature, and local velocity gradient. The lowest temperature included in these tables is 10 K, but to allow us to handle very cold molecular gas we have extended them down to 5 K using collisional data from Flower (2001) and Wernli et al. (2006), as described in Appendix A of Glover & Clark (2012). The LVG calculation in Neufeld & Kaufman (1993) and Neufeld et al. (1995) assumes that CO is excited primarily by collisions with H_2. However, in our cooling function, we also account for collisions with atomic hydrogen and with electrons, using the procedure described in section C.4 of Meijerink & Spaans (2005).

Table B1. Processes included in our thermal model.

Process	Reference(s)
Radiative cooling:	
C fine structure lines	Atomic data – Silva & Viegas (2002)
	Collisional rates (H) – Abrahamsson, Krems & Dalgarno (2007)
	Collisional rates (H_2) – Schroder et al. (1991)
	Collisional rates (e^-) – Johnson, Burke & Kingston (1987)
	Collisional rates (H^+) – Roueff & Le Bourlot (1990)
C^+ fine structure lines	Atomic data – Silva & Viegas (2002)
	Collisional rates (H_2) – Flower & Launay (1977)
	Collisional rates (H, $T < 2000$ K) – Hollenbach & McKee (1989)
	Collisional rates (H, $T > 2000$ K) – Keenan et al. (1986)
	Collisional rates (e^-) – Wilson & Bell (2002)
O fine structure lines	Atomic data – Silva & Viegas (2002)
	Collisional rates (H) – Abrahamsson et al. (2007)
	Collisional rates (H_2) – see Glover & Jappsen (2007)
	Collisional rates (e^-) – Bell, Berrington & Thomas (1998)
	Collisional rates (H^+) – Pequignot (1990, 1996)
Si fine structure lines	All data – Hollenbach & McKee (1989)
Si^+ fine structure lines	Atomic data – Silva & Viegas (2002)
	Collisional rates (H) – Roueff (1990)
	Collisional rates (e^-) – Dufton & Kingston (1991)
H_2 rovibrational lines	Glover & Abel (2008)
CO rovibrational lines	Neufeld & Kaufman (1993), Neufeld, Lepp & Melnick (1995)
Gas-grain energy transfer	Hollenbach & McKee (1989)
Atomic resonance lines	Hydrogen – Black (1981), Cen (1992)
	Helium and metals – Gnat & Ferland (2012)
Atomic metastable transitions	Hollenbach & McKee (1989), Baczynski, Glover & Klessen (2015)
Compton cooling	Cen (1992)
Chemical cooling:	
H collisional ionization	See Table A1
H_2 collisional dissociation	See Table A1
H^+ recombination	Ferland et al. (1992), Wolfire et al. (2003)
Heating:	
Photoelectric effect	Bakes & Tielens (1994), Wolfire et al. (2003)
H_2 photoionization	Meijerink & Spaans (2005)
H_2 photodissociation	Black & Dalgarno (1977)
UV pumping of H_2	Burton, Hollenbach & Tielens (1990)
H_2 formation on dust grains	Hollenbach & McKee (1989)
X-ray Coulomb heating	See Section 2.3.2
Cosmic ray ionization	Goldsmith & Langer (1978)

This paper has been typeset from a TEX/LATEX file prepared by the author.